



Available online at www.sciencedirect.com

ScienceDirect

journal homepage: www.elsevier.com/locate/bbe



Original Research Article

Fuzzy genetic-based noise removal filter for digital panoramic X-ray images



Mehravar Rafati^a, Fateme Farnia^a, Mahdi Erfanian Taghvaei^b,
Ali Mohammad Nickfarjam^{c,*}

^a Department of Medical Physics and Radiology, Faculty of Paramedicine, Kashan University of Medical Sciences, Kashan, Iran

^b Department of Dentistry, Kashan University of Medical Sciences, Kashan, Iran

^c Department of Computer Engineering, Faculty of Electrical and Computer Engineering, University of Kashan, Kashan, Iran

ARTICLE INFO

Article history:

Received 30 April 2018

Received in revised form

6 July 2018

Accepted 16 August 2018

Available online 5 September 2018

Keywords:

Orthopantomography images

Genetic algorithm

Poisson noise

Anscombe transformation

ABSTRACT

This paper proposed a novel fuzzy genetic-based noise removal filter and surveyed the gain of popular filters for noise removal in the digital orthopantomography (OPG) images. The proposed filter is a non-invasive technique for attaining sub-clinical information from the areas of interest in each tooth, both jaws and maxillofacial.

The proposed Poisson removal filter combines 4th-order partial differential equations (PDE), total variation (TV) and Bayes shrink threshold accompanied by fuzzy genetic algorithm (FGA) and the exact unbiased inverse of generalized Anscombe transformation (EUIGAT). Experiments were performed in order to show the effect of noise removal filters on 110 simulated, 106 phantom and 104 panoramic radiographic images for subjects (aged 30–60 years old, 50 males and 54 females). Various noises degraded filters and Canny edge detection was performed separately in three kinds of images. The program measured mean square error (MSE), peak signal to noise ratio (PSNR), image quality index (IQI), structural similarity index metric (SSIM) and figure of merit (FOM).

The results verify that the proposed filter enhances physicians' and dentists' skill of diagnosing normal and pathological events in the teeth, jaws, temporomandibular joint (TMJ) regions and changeable anatomical panoramic landmarks related to osteoporosis progress in the mandible bone using noise removal and improving images quality. Experimental results show the superiority of this filter over other noise removal filters.

© 2018 The Authors. Published by Elsevier B.V. on behalf of Nalecz Institute of Biocybernetics and Biomedical Engineering of the Polish Academy of Sciences. This is an open access article under the CC BY license (<http://creativecommons.org/licenses/by/4.0/>).

* Corresponding author at: Department of Computer Engineering, Faculty of Electrical and Computer Engineering, University of Kashan, Kashan, Iran.

E-mail addresses: afshin_rft@yahoo.com (M. Rafati), ftm.frn@gmail.com (F. Farnia), mehdierfania60@yahoo.com (M.E. Taghvaei), amnicksfarjam@grad.kashanu.ac.ir (A.M. Nickfarjam).

<https://doi.org/10.1016/j.bbe.2018.08.005>

0208-5216/© 2018 The Authors. Published by Elsevier B.V. on behalf of Nalecz Institute of Biocybernetics and Biomedical Engineering of the Polish Academy of Sciences. This is an open access article under the CC BY license (<http://creativecommons.org/licenses/by/4.0/>).

1. Introduction

Over past three decades, conventional radiography is replete with more electronic equipments and computational programs. These appendices have become effective alternatives due to their great impact on image quality and workflow such as replacing traditional photographic films with digital X-ray detectors. This replacement caused higher time efficiency, a better digital transition and images enhancement [1]. In addition, though using less radiation, the resulting image has the same contrast as conventional radiography. It also offers other advantages including instantaneous image preview and access, a wider dynamic access to over-and under-exposure, deletion film processing steps and possibility of using special processing techniques which enhance image quality [1]. Recently, orthopantomography (OPG) has expanded to be one of the main supplementary trials in dentistry. It is a view of lower face which shows all the teeth of upper and lower jaws with their number, position and growth. Besides, OPG has more benefits than radiography of individual teeth [2,3].

The problems with the jaw bone and temporomandibular joint (TMJ), the joint which connects the jaw bone to the head, are possible to be diagnosed in this radiography [2]. An OPG can be effective in planning orthodontic treatment and diagnosing of wisdom teeth. OPG is widely used to produce a comprehensive survey of the maxillofacial complex and as a useful tool in the primary trial of osteoporosis [4]. Gaussian, Poisson, speckle and salt-and-peppers are different types of noises which cause by various sources in the transmission system and environmental factors [5]. Therefore, X-ray images have a statistical nature, because they are produced by digital receptors [6]. Poisson noise is one of the major noises which on one hand, quality of X-ray images degraded; because of being close to discrete photons nature. On the other hand, smoothing images is necessary to remove the noise by standard filters that also can preserve the edges [7]. Both linear and nonlinear conventional filtering methods reduce noises by smoothing the image and may also smooth edge information [8]. Besides, data can be transformed to the space domain or frequency domain for filtering the bandwidth, which should be determined precisely. If the bandwidth becomes narrow or wide, the noise cannot be decreased well or some information will be omitted. It seems that they have no proper filtering effects [9,10].

Partial differential equations-based methods (PDE) utilize the heat conduction and control on diffusion direction which can preserve the edge information. It is important that the noise reduced and edge details can be preserved precisely [11]. The major substantial tools for denoising in medical image are the total variation (TV) model suggested by Rudin et al. and the proposed model of Perona and Malik based on anisotropic noise smoothing [12,13]. Deledalle et al. suggested a non-local mean algorithm with iterative characteristic of Poisson noise reduction in X-ray images [14]. Another survey was proposed a combined method including block matching and three dimensions filtering (BM3D). They concluded that the performance of spatial domain for Gaussian noise reduction is more useful than other filters [15]. Makitalo et al. showed that Anscombe transform stabilized the variance of Poisson noise

and then, adjusted BM3D [16]. Wang et al. proposed Bayes shrink threshold using Daubechies wavelet transform for denoising in medical images [17]. In another study, median filtering was better than Gaussian and finite impulse response (FIR) filtering for speckle and Poisson noises in dental X-ray images [18]. Du et al. showed that the performance of dual tree complex wavelet transform (DTCWT) is more proper than wavelet transform for Poisson noise reduction from X-ray images [19]. Jisha et al. presented that a hybrid of curvelet transform and variance stabilization transform is better than wavelet transforms for Poisson denoising [20].

Fuzzy genetic algorithm (FGA) is inspired by nature-based evolutionary process and has popularity in different fields of medicine [21]. Due to the importance of OPG images in diagnosis and therapeutic measures, oral and maxillofacial surgery, fractures and extraction for evaluating parameters of osteoporosis in the mandible, the proposed filter combines 4th-order PDE, TV and Bayes shrink threshold for optimum noise reduction and edge preservation in OPG images. This combination is accompanied by the fuzzy genetic algorithm in order to exact unbiased inversed (EUI) of generalized Anscombe transformation with other denoising filters. This method may provide physicians and dentists with useful information about injuries of oral and maxillofacial regions through enhancing image quality.

2. Material and method

2.1. Related works

This section is dedicated for related denoising filters which are utilize for comparison with the proposed FGA-based noise removal filter.

2.1.1. Poisson noise removal techniques

This kind of noise is generated from nonlinear response of detectors with Poisson distribution. The image information is dependent on detection and recording of the electron random emission in a circuit or the photon in an optical device with Poisson distribution and specified average value. Since in the Poisson distribution, the mean is equal to the variance and the signal containing data is completely dependent on the standard deviation. So, the higher the standard deviation, the more noise is added to the signal [22]. The probability distribution of a Poisson random variable X representing the number of successes occurring in a given time interval or a specified region of space which is given as:

$$f(X) = \frac{e^{-\lambda} \times \lambda^x}{x!} \quad (1)$$

where x is the exact number of successes, e equals 2.71828, λ is the mean number of successes in the given time interval or region space and $x!$ is the factorial of x [23]. The model of reduction due to Poisson noise is:

$$u(i, j) = \frac{1}{\lambda} \text{Poisson}(\lambda \times t(i, j)) \quad (2)$$

where $t(i, j)$ and $u(i, j)$ are original and degraded images, respectively. The argument of the Poisson function is related to the mean of the Poisson distribution which the return value explains a Poisson random generation function based on Poisson random numbers. Since the degree of corruption is based on the amounts of detected photons, poor photons signify shorter λ [23]. Several filters are practical for Poisson noise reduction. Some obtain visual perception and others get suitable noise suppression or smoothing capability. Popular noise removal filters are presented in this section and corresponding equations are introduced in Table 1. Also, abstract algorithm used for each presented filter has been given in Table 1.

2.1.2. Mean filter

The mean filter is an uncomplicated, perceptive and clear method to complete image smoothing. It substitutes the center value with average of surrounding the pixel values surrounding in the window [24,25].

2.1.3. Median filter

The Median filter is a nonlinear noise reduction which runs through the image pixel and changes each pixel with the median of its surrounding pixels [26,27].

2.1.4. Weighted median filter

The weighted median is similar to median filtering. But, it has the mask that is not empty and consists of some weight or average values. Researches verify high performance of weighted median for low density noise [28,29].

2.1.5. Weiner filter

This filter is used for optimizing the mean square error (MSE) in corrupted images by additive noise and blurring [30,31].

2.1.6. Frequency-domain filter

It is a kind of filtering function which consists of special frequency elements for signal handling. Fourier filter applied Fourier transform on the signal; then, attenuated and compensated special frequencies and eventually the results transformed inversely. There are different kinds of Fourier filters such as the Ideal, Butterworth and Gaussian filters [32,33].

2.1.7. Wavelet-based denoising

The wavelet thresholding follows three steps. First, it calculates the discrete wavelet transform (DWT) of the medical images. Second, this filter assigns threshold for the wavelet coefficients. Third, it calculates the inverse discrete wavelet transform (IDWT) for estimating denoised values. The wavelet transform has high performance for denoising; because of its characteristics such as multi-resolution and multi-scale properties. Threshold may be non-adaptive such as Visu shrink and adaptive such as Stein's unbiased risk estimator (SURE) shrink, Bayes shrink and cross validation [34,35].

2.1.7.1. Visu shrink. It is a non-adaptive universal threshold which is based on the number of data points. Visu shrink performance is in terms of MSE when the value of pixels is infinite [36].

2.1.7.2. SURE shrink. It is a universal thresholding which operated on sub-band adaptive shape by minimizing Stein's biased risk estimator [37].

2.1.7.3. Bayes shrink. Bayes shrink is an adaptive threshold which minimizes the Bayes risk estimator function with assuming generalized Gaussian distribution for each sub-band [38,39].

Table 1 – Explanation and equations of comparing noise reduction filters.

Filter type	Formula	Parameter
Mean	$J(x, y) = \frac{1}{p \times q} \sum_{(s,t) \in S_{xy}} I(s, t)$	$J(x, y)$ is response of mean filter in x and y orientations. p and q indicate number of rows and columns of filter's neighborhood. S_{xy} shows region with size of $p \times q$ (window or mask with this size) from input noisy image (I). s and t are central orientations from the region in (x, y) [24-27].
Median Weighted median	$J(x, y) = \text{median}_{(s,t) \in S_{xy}} \{I(s, t)\}$ $B = \text{median}(w_1 \diamond \text{sgn}(w_1)A_1, \dots, w_N \diamond \text{sgn}(w_N)A_N)$	$B; A_1, A_2, \dots, A_N$ and w_1, w_2, \dots, w_N are outputs of weighted median filter, input samples, set of real amounts weight, respectively. \diamond is a replication operator where sgn is the signs of weighted that are capability to couple with the input samples [28,29].
Weiner	$J(w, v) = \left[\frac{H(w, v)^*}{H(w, v)^2 + \frac{S_n(w, v)}{S_s(w, v)}} \right] I(w, v)$	$J(w, v)$ and $I(w, v)$ are filtered and original images, respectively. $H(w, v)$ is the destructive function ($*$ shows complex conjugate) where $S_n(w, v)$ and $S_s(w, v)$ are power spectra of the noise and the original image [30,31].
Ideal Fourier	$H(s, t) = \begin{cases} 1 & \text{if } L(s, t) \leq L_0 \\ 0 & \text{if } L(s, t) > L_0 \end{cases}$	L_0 is a definite non-negative number. $L(s, t)$ is the interval from (s, t) to the center for the Fourier-transform filters [32,33].
Butterworth Fourier	$H(s, t) = \frac{1}{1 + L(s, t)/L_0 ^{2n}}$	
Gaussian Fourier	$H(s, t) = e^{-L^2(s, t)/2L_0^2}$	

Table 1 (Continued)

Filter type	Formula	Parameter
SURE shrink wavelet	$T_{SURE} = \min(u, \sigma\sqrt{2\log M})$	M, u and σ are the number of wavelet coefficients in specified sub-bands, the amount that minimizes SURE and noise standard deviation, respectively [37].
Bayes shrink wavelet	$\sigma_y^2 = \sigma_x^2 + \sigma_z^2; \sigma_z^2 = \left[\frac{\text{median}(HH_1)}{0.6745}\right]^2; \sigma_y^2 = \frac{1}{M} \sum_{m=1}^M A_m^2; T_B = \begin{cases} \frac{\sigma_z^2}{\sigma_x^2} & \text{if } \sigma_z^2 < \sigma_y^2 \\ \max\{ A_m \} & \text{otherwise} \end{cases}$	σ_y, σ_x and σ_z are standard deviations of wavelet transform of the destructive image (Y), original image (X) and the noise amounts (Z) based on Gaussian distribution, respectively. HH_1 is the 1st decomposition level diagonal sub-band where 0.6745 is the experimental amount. A_m^2 and M are the wavelet coefficients and the total number of wavelet coefficient in that sub-band, respectively. T_B is Bayes shrink threshold and $\sigma_x = \sqrt{\max(\sigma_y^2 - \sigma_z^2, 0)}$ [38,39]. σ is noise standard deviation and N is the pixel's number in the image [36].
Visu shrink wavelet	$T_{visu} = \sigma\sqrt{2\log N}$	$GCV_t^u(\delta)$ is generalized cross validation in level u , component t and threshold δ . N_t^u is upper bound for optimal threshold where $N_{t_0}^u$ is the number of zero elements. w_t^u is the vector of wavelet coefficients at level u and component t where $w_{t,\delta}^u$ is the shrunk coefficients in the threshold δ [40].
Cross validation	$GCV_t^u(\delta) = \frac{\frac{1}{N_t^u} \ w_t^u - w_{t,\delta}^u\ ^2}{\left \frac{N_{t_0}^u}{N_t^u}\right ^2}$	$u(x, y, t)$ presents an image with directions (x, y) at time t ; $D(x, y, t)$ is the diffusion coefficient, ∇ explains the gradient operator and div indicates to the divergence operator. For inhomogeneous diffusivity, Perona–Malik introduced D function. k is a factor for managing the gradient of the image [41–45]. D and u were introduced in previous PDE. ∇^2 is the Laplacian of the image u . Since, it will be zero if the image becomes planar. Therefore, we need an energy function. Ω and ∇^2 indicates to the image support and Laplacian operator, respectively. For planar image should be $ \nabla u^2 = 0$ until $E(u)$ becomes minimum. $E(u)$ is energy function [41–45].
2nd order PDE	$\frac{\partial u(x,y,t)}{\partial t} = \text{div}(D(x, y, t)\nabla u(x, y, t))$ $u(x, y, 0) = u_0(x, y)$ $D(x, y, t) = \frac{1}{1 + \frac{ \nabla u ^2}{k^2}}$	
4th order PDE	$\frac{\partial u}{\partial t} = -\nabla^2 [D(\nabla^2 u)\nabla^2 u]$ $E(u) = \int_{\Omega} f(\nabla u^2) \partial_x \partial_y$	
Complex diffusion	$u_t = \text{div}(D(u_m(u)\nabla u))$ $D(u_m(u)) = \frac{e^{i\theta}}{1 + \left(\frac{u_m(u)}{k}\right)^2}$	u_t is an image at time t that provided from both real and imaginary planes. div indicates the divergence operator and D is diffusion coefficient. u_m is an image that is accompanied with Schrodinger equations. ∇ is the gradient operator. e and i are exponential function and complex number symbols, respectively. k is the threshold factor where θ is phase angle [45]. $i, j = 1, \dots, N$ and y is a two dimensional signal. $V(y)$ is the total variation. Since, above the mentioned function is isotropic and non difference, it is relevance to minimize using an anisotropic form. V_{ansio} is the total variation with anisotropic version. E is the two dimensional L^2 norm. In bracket of $E(x, y)$, x is an input signal and y is an approximation from x that has less total variation compared to x ; but is near to x . λ is regularization parameter. $\lambda > 0$ manages the degree of smoothing [46,47].
TV	$V_y = \sum_{ij} \sqrt{ y_{i+1,j} - y_{i,j+1} ^2 + y_{i,j+1} - y_{ij} ^2}$ $V_{ansio}(y) = \sum_{ij} \sqrt{ y_{i+1,j} - y_{ij} ^2 + y_{ij+1} - y_{ij} ^2}$ $V_{ansio}(y) = \sum_{ij} y_{i+1,j} - y_{ij} + y_{ij+1} - y_{ij} $ $\min_y E(x, y) + \lambda V(y)$	$V(y)$ is the total variation. Since, above the mentioned function is isotropic and non difference, it is relevance to minimize using an anisotropic form. V_{ansio} is the total variation with anisotropic version. E is the two dimensional L^2 norm. In bracket of $E(x, y)$, x is an input signal and y is an approximation from x that has less total variation compared to x ; but is near to x . λ is regularization parameter. $\lambda > 0$ manages the degree of smoothing [46,47].
SFPD	$\bar{D}_{\alpha x}(u) = D_{\alpha x} u(x + \frac{x}{2}, y) \leftrightarrow \left[\frac{1 - \exp(i2\pi f_1 h/m)}{h} \right]^\alpha \exp(i\pi \alpha f_1/m) U(f_1, f_2)$	u is digital image with size $m \times m$ pixels. x and y are directional ways of operator. α indicates a real number and h is the sub-pixel operator size. $\bar{D}_{\alpha x}(u)$ is the central differentiation for the SFPD where $D_{\alpha x} u$ is a fractional order derivative operator that is accompanied with $u(x, y)$ indicates to a period boundary. $U(f_1, f_2)$ is two dimensional discrete Fourier transform of $u(x, y)$ and f_1, f_2 are frequency bounds. “ \leftrightarrow ” illuminates the Fourier transform pair. The \exp and i are exponential and complex number symbols, respectively. The pi number equals 3.14. Likely, $\bar{D}_{\alpha y}(u)$ can be extracted from this manner [48].

2.1.7.4. *Cross validation.* It substitutes wavelet coefficients with weighted average of neighborhood coefficients by minimizing generalized cross validation function in order to optimize the threshold in each coefficient [40].

2.1.8. *PDEs-based noise reduction*

These kinds of filters are based on iterative procedures for denoising in medical images. Their basis is originated from PDE in which the diffusion processes are not uniformly through images. As a matter of fact, their smoothing processes are adapted on the image elements. There are three developed PDEs-based methods such as 2nd order, 4th order and complex diffusions [41–45].

2.1.9. *TV-based denoising*

It is an iterative method for enhancing medical images. The TV calculates the differentiation between variances of two pixels. It substitutes normal variance pixel with high variance pixel in the medical image [46,47].

2.1.10. *Sub pixel fractional order difference (SFPD)-based noise reduction*

It is an incremental function of the fractional extraction for absolute amount of the image intensity function using Euler–Lagrange equation and then, calculates the SFPD in frequency region [48].

2.1.11. *Proposed FGA-based noise removal filter*

The proposed method of this study is based on the combination of TV, Bayes shrink and 4th-order PDE that are optimized using the fuzzy genetic algorithm. This combination is a weighted combination. Thus, the three-way weighted combination of the three filters is used to create the final image. First, the output image of each filter is fragmented and a coefficient is specified for each part. Wherever necessary, the weight of each filter, which has the best response compared to the other two filters in the desired part, will improve the final output. For example, if in the n th segment, the TV filter output has more appropriate response than others, the weight of the TV filter will increase the n th segment. Experimental images used in this research are digital panoramic X-ray images and the predominant noise of test images is Poisson noise which is not independent of signal. Therefore, in order to increase the efficiency of the suggested filter in noise elimination, first, a pre-processing step is performed on test images using the EUGAT function [16,49].

$$J_{EUGAT}(T) = \frac{1}{4}T^2 + \frac{1}{4}\sqrt{\frac{3}{4}}T^{-1} - \frac{11}{8}T^{-2} + \frac{5}{8}\sqrt{\frac{3}{2}}T^{-3} - \frac{1}{8}\sigma_n^2 \quad (3)$$

where $J_{EUGAT}(T)$ is an approximation which is close to the function of EUGAT and T is noisy image which has Poisson noise. σ_n^2 is noise variance of the observed data.

After pre-processing step, the output of the function is given which utilized as input of three filters and finally, I_{Bayes} , $I_{4th-orderPDE}$ and I_{TV} obtained. Now, three images in the weighted compilation should be optimized using the fuzzy genetic algorithm to achieve a high-quality image without noise in the output.

The three images are divided into smaller parts. Suppose the image dimensions are $P \times Q$ and $p \times q$ is selected as dimensions of each image segments. Depending on the image dimensions and the dimensions chosen for each image segment; the image is divided into mn smaller parts ($P = n \times p$, $Q = m \times q$). The parameters p and q depend on how often the work is done. In high frequencies $p = q = 41$, in medium frequencies $p = q = 23$ and in low frequencies $p = q = 9$ are considered [50]. The output images of Bayes shrink, TV and 4th order PDE methods are called I_{TV} , I_{Bayes} and $I_{4th-orderPDE}$, respectively. Their different segments can be represented by $ITV_{i,j}$, $IBayes_{i,j}$ and $I_{4th-orderPDE_{i,j}}$ where $i \in \{1, \dots, n\}$ and $j \in \{1, \dots, m\}$. The fuzzy genetic algorithm creates three populations with $m \times n$ size as primary population that each population is related to I_{TV} , I_{Bayes} or $I_{4th-orderPDE}$. The population associated with I_{TV} , I_{Bayes} and $I_{4th-orderPDE}$ are P_{ITV} , P_{IBayes} and P_{IPDE} , respectively. Each population contains K chromosomes and the chromosome k is represented by $P_{ITV}(k)$, $P_{IBayes}(k)$ and $P_{IPDE}(k)$. Each of the chromosomes $P_{ITV}(k)_{i,j}$, $P_{IBayes}(k)_{i,j}$ and $P_{IPDE}(k)_{i,j}$ has $m \times n$ genes where $i \in \{1, \dots, n\}$ and $j \in \{1, \dots, m\}$, respectively.

Using a multiplication of randomly generated weights in the initial population for each parts of the image, denoised image is created using (4).

$$\begin{aligned} \text{Denoised image} = & P_{ITV}(k)_{i,j} \times ITV_{i,j} + P_{IBayes}(k)_{i,j} \times IBayes_{i,j} \\ & + P_{IPDE}(k)_{i,j} \times I_{4thorderPDE_{i,j}} \end{aligned} \quad (4)$$

After obtaining a denoised image, it is easy to find out that intensity values may be higher than 255. Therefore, intensity values normalized in $\{0, \dots, 255\}$ based on min-max normalization method [51].

$$\begin{aligned} \text{Normalized denoised image} \\ = \frac{\text{denoised image} - \min(\text{denoised image})}{\max(\text{denoised image}) - \min(\text{denoised image})} \times 255 \end{aligned} \quad (5)$$

Therefore, the fitness of normalized denoised image can be determined. To determine the image fidelity, sequential connected component labeling (SCCL) method is used [52,53]. This algorithm defines the regions of the input image (I) and normalized denoised image for the k th chromosome. In fact, the more similar the various areas of the two images are, the higher the fitness is. To apply SCCL to each input image (I) and normalized denoised image; both images are initially converted to the binary mode and the SCCL method is applied to both images. The number of pixels labeled identical in both images (in the same region) specifies the degree of the denoised image fitness.

The proposed method uses fuzzy genetic approach which is presented by Djellali and Adda [54]. This process is performed for all k chromosomes in the population. Therefore, k -images and k -fitness values associated with them will be on hand. By choosing the best fitness function, the most suitable chromosome is chosen. By the Roulette wheel method, new chromosomes are constructed using the appropriate chromosomes of the current population. The number of new chromosomes will also be k -cases in addition to the previous chromosomes will

have 2^k -chromosome. So far, new population has been created and fitness value for each of the chromosomes has been determined. The goal is to achieve a better generation with the advancement of population. Thus, chromosomes that have higher fitness values will be selected for cross over procedure [55].

After selecting two chromosomes from the population for cross over, a single-point compound is used to produce two offsprings from two parents [56,57]. In a single point cross over, a gene from the chromosome is randomly selected as the intersection point and two parents are combined from the point. In the proposed FGA-based noise removal approach, the trend for using one-point combination continues to the extent that the number of new chromosomes is equal to that of the previous population.

In addition, mutation procedure was used in this study which the offsprings have one or more characteristics that are not related to any parent. The main goal of the mutation is that by changing the genomes of the chromosomes, search in the response space done in a way that prevents early convergence in local optimizations [58]. The method of making a mutation is that a random number is generated and if the number be greater than mutation probability, the mutation done. $Prob_{mu}$ shows mutation probability. More precisely, if the random number obtained for the chromosome be greater than $Prob_{mu}$, the mutation performed. Since the probability of a genetic mutation in nature is very low, $Prob_{mu}$ usually selects a large number. In the proposed method, $Prob_{mu}$ is considered equal to 95%. After some generations passed, a population produced which each chromosome represents the cost-effective predictors. This genetic variation search-based optimization approach creates a variables subset until there is no improvement of model accuracy. In order to evaluate potential solution optimality, Fuzzy ART1 Wrapper model is used [54].

Now, k -chromosomes from the previous population and the new k -chromosomes make population for the next iteration. Therefore, the chromosomes are arranged in a descending order according to the fitness value and the k -chromosomes are selected from the list of 2^k -chromosomes. Genetic steps are repeated in a definite number and, finally, the best chromosomes are selected along with the best images. Proposed FGA-based denoising approach and comparing methods are summarized in Fig. 1.

2.2. Experimental results

In this section, the results of the proposed denoising method are illustrated and compared with other related approaches which are mentioned in Section 2. This method was applied to simulated images, phantom and real radiographs. Five criteria are utilized for performance evaluation. Also, a criterion which shows appropriate visual perception detects edges improvement.

2.2.1. Edge detection

Edge detection is laborious in noisy radiographs; because both noises and edges include high frequency elements. There are two general kinds of operators for edge detection. First, gradient-based operators such as Sobel, Prewitt, Roberts, and Canny that use the first-derivative of images for finding the maximum and minimum intensities. The other is based

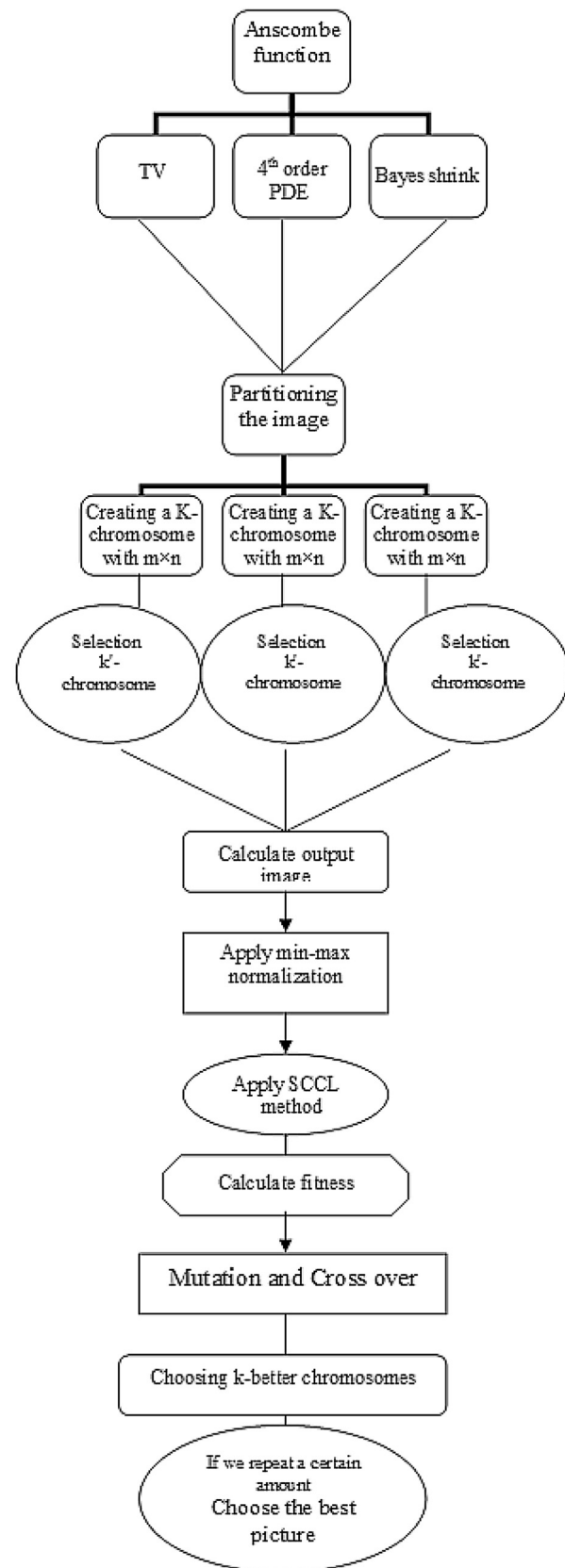


Fig. 1 – Flowchart of the proposed approach.

on second-derivative such as Laplace of Gaussian (LoG) and zero-crossing. Proper edge detection should provide some features such as fruitful evaluation from magnitude and orientation of the edges, high rate for tracing and desirable localization. This paper utilizes Canny edge detector for present study [58,59].

Canny detector is a multi-step operator for tracing a broad range in images. Its procedure includes four stages. First, a Gaussian filter smoothens the image for noise removal. Second, local maximum gradient of image should be found. Next, Canny uses two thresholds for tracing potential edges. Finally, this edge detection quenches either weak edges or non-connected edges to the strong edge [60].

2.3. Dataset

Three kinds of datasets of the images are utilized for the proposed FGA-based noise removal approach evaluation.

2.3.1. Simulated images

We have made a certain number of simulated radiographies of 512 pixels. At first, a coefficient map with coefficients which decrease from 100% for rightmost pixel to 0% for leftmost one is generated. Afterward, some various geometrical shapes including circles and rectangles are added which have random positions near the map. Radius of circles and sides of rectangles are randomly selected in $\{1, \dots, 512\}$. When geometrical shapes are added to their map, a random number between 0 and 100% is added to them. In this case, the number which is more than 100% is replaced by 100%. According to Poisson statistics, noises are added to each pixel independently. Then, the map is filtered by all noise removal filters whose corresponding window sizes are small (9×9), medium (23×23) and large (41×41) [61]. The number of noise was added to the images artificially as 10,000. The datasets consisted of 110 radiograph images for simulation.

2.3.2. Phantom and real radiographs

The Phantom used in this study was consisted of bone, soft tissue and fat. For this purpose, anthropomorphic skull and paraffin were applied with different amounts of NaCl as impurity. Paraffin wax with general formula of C_nH_{2n+2} and average density of 0.9 g/cm was applied to soft tissue. This phantom has been introduced comprehensively in our previous study [62]. This phantom is used in order to cover a fixed anatomical shape of the face for evaluating the performance of filters in noise reduction. It should be mentioned that it was done for different anatomical shapes of the face in real subjects. Panoramic images were obtained from the phantom. All subjects conceded their informed written consent for the examinations using digital OPG machine (Planmeca, ProOne, Helsinki, Finland). For attaining a standard situation and elimination inter-observer variability, the images were taken by one operator at 8-16 mA and 2-10 s; the voltage varied between 60 and 70 kVp based on age, sex and anatomical shape of subjects' face.

Present study was accepted by the Ethics Committee of Kashan University of Medical Sciences in Iran. They were aged 30-60 years old (54 males and 50 females). The datasets

consisted of radiographs for 106 and 104 for the phantom and real radiographic samples, respectively compiled by a panoramic system. They were positioned in the OPG system in which the vertical line was adjusted with the samples Sagittal plane and Frankfort plane parallel to the floor. The images were taken by charge coupled device (CCD) and optical fiber digital sensor and the data were compiled in the computer of panoramic system. Tagg image file format (TIFF) was used to take the images of the maxillofacial region from hard drive. Then, this was delivered to a personal computer for post-processing. An algorithm was developed and used to contribute to the understanding of the process (Fig. 1). The program was designed using MATLAB software (version 7.01; Mathworks; USA) to derive images in TIFF format. Matlab depicted images with dimensions equal to 2837×1435 pixels.

2.4. Performance criteria

In order to assess results of the proposed method compared to the other filters in terms of noise removal, some performance criteria are used which explained shortly as follows.

2.4.1. Mean square error (MSE)

It was used for averaging the square of the differentiation between the intensity values of the original and denoised images. Lower MSE value is associated with minimum difference between them. The range of MSE is $[0, \dots, 1]$ [63].

$$MSE = \frac{1}{MN} \sum_{i=1}^M \sum_{j=1}^N (x(i,j) - y(i,j))^2 \quad (6)$$

where $x(i, j)$ and $y(i, j)$ represent the original and denoised images, respectively. Also, i and j are pixel situation in $M \times N$ image.

2.4.2. Peak signal noise ratio (PSNR)

This metric parameter gives a fraction between the maximum strength of the signal and the noise elements. Higher PSNR value exhibits more proper image quality. PSNR value range is $[0, \dots, 1]$ [64].

$$PSNR = 10 \log_{10} \frac{(2^n - 1)^2}{\sqrt{MSE}} \quad (7)$$

where n shows the number of bits used for introducing pixel of the radiograph. In this regard, n equals 8 for gray level image.

2.4.3. Image quality index (IQI)

This image quality index displays the degree of disturbance of the radiograph using factors such as lack of correlation, lightness and contrast distortions. Similar to MSE and PSNR criteria, IQI range is $[0, \dots, 1]$. Lower disturbances are defined with the IQI values when they are near 1 [64].

$$IQI = \frac{4 * \sigma_{xy} * \bar{x} * \bar{y}}{(\sigma_x^2 + \sigma_y^2) * ((\bar{x})^2 + (\bar{y})^2)} \quad (8)$$

\bar{x} , \bar{y} , σ_x^2 , σ_y^2 and σ_{xy} are given as:

$$\bar{x} = \frac{1}{N} \sum_{i=1}^N x_i \tag{9}$$

$$\bar{y} = \frac{1}{N} \sum_{i=1}^N y_i \tag{10}$$

$$\sigma_x^2 = \frac{1}{N-1} \sum_{i=1}^N (x_i - \bar{x})^2 \tag{11}$$

$$\sigma_y^2 = \frac{1}{N-1} \sum_{i=1}^N (y_i - \bar{y})^2 \tag{12}$$

$$\sigma_{xy} = \frac{1}{N-1} \sum_{i=1}^N (x_i - \bar{x})(y_i - \bar{y}) \tag{13}$$

2.4.4. Structural similarity index metric (SSIM)

It is a similarity index for comparing original and denoised radiographs using luminance, contrast, and structure. If we expect appropriate similarity, its value should be near 1 [65,66].

$$SSIM = \frac{(2*\bar{x}*\bar{y} + C_1)(2*\sigma_{xy} + C_2)}{(\sigma_x^2 + \sigma_y^2 + C_2)*((\bar{x})^2 + (\bar{y})^2 + C_1)} \tag{14}$$

\bar{x} , \bar{y} , σ_x^2 , σ_y^2 and σ_{xy} are given as:

$$\bar{x} = \frac{1}{N} \sum_{i=1}^N x_i \tag{15}$$

$$\bar{y} = \frac{1}{N} \sum_{i=1}^N y_i \tag{16}$$

$$\sigma_x^2 = \frac{1}{N-1} \sum_{i=1}^N (x_i - \bar{x})^2 \tag{17}$$

$$\sigma_y^2 = \frac{1}{N-1} \sum_{i=1}^N (y_i - \bar{y})^2 \tag{18}$$

$$\sigma_{xy} = \frac{1}{N-1} \sum_{i=1}^N (x_i - \bar{x})(y_i - \bar{y}) \tag{19}$$

$C_1 = (k_1D)^2$, $C_2 = (k_2D)^2$ are two variant values to stabilize the division with poor divisor. D equals the dynamic range of pixel-values (generally this is 2 number of bits per pixel⁻¹) where $k_1 \ll 1$ and $k_2 \ll 1$ are two scalar constants.

2.4.5. Figure of merit (FOM)

This parameter measures the capability of edge conservation of the radiograph. The values range of the FOM is [0, . . . , 1] [45].

$$FOM = \frac{1}{\max(N_n \times N_o)} \times \sum_{i=1}^{N_o} \frac{1}{1 + d_E^2 \times \lambda} \tag{20}$$

where the N_n and N_o are pixels of the edge in terms of denoised and original images, respectively. Also, d_E is the Euclidean distance between i th edge pixel in the radiograph which corrupted with noise and nearest edge pixel in basic image.

3. Results

The mean ± standard deviation (SD) values were observed on the data. We used the Kolomogrove–Smirnov and Levene tests for evaluating normal and homogeneity of variance, respectively. To insure the significance of the means in terms of MSE, PSNR, IQI, SSIM and FOM for all filters and edge detection, the analysis of variance (ANOVA) was used. The post hoc test Tukey was used in the present study which $P < 0.05$ was considered as significant. For analyzing the data, SPSS software (SPSS V.11.5, Inc., Chicago, IL) was used.

The results of the noise removal filters and Canny edge detection are summed up in Figs. 2–4. Table 2 demonstrates the effects of noise reduction accompanied by image enhancement on the simulated, phantom and real radiographic images using the proposed and other filters. Performance criteria utilized in this study have some advantages such as ability to provide fast, suitable and simple situation for quantifying the errors objectively [65], monotonously increment without differentiation of the image fidelity between the base and changeable versions of the corrupted radiograph [66], greater accuracy and consistency compared to the other metric parameters [66].

Lower MSE values signify a higher image similarity, whereas smaller values in terms of PSNR, IQI, SSIM and FOM signify a lower image similarity [65]. There were significant differences in terms of MSE, PSNR, IQI, SSIM and FOM among applied canny edge detectors to the proposed method and comparing filters' results ($P < 0.05$). Tables 3–5 demonstrate the lowest MSE and highest PSNR, IQI, SSIM and FOM for evaluating noise reduction accompanied by image quality increment using three kinds of datasets of images (simulation, phantom, and real images). For the overall evaluation of the image quality, especially the superior and inferior borders of the cortex, mandibular cortical thickness (MCT), and mental foramen; five experienced dentists and maxillofacial surgeons confirmed better performance of the proposed method compared with other filters. Besides, the proposed method results were assessed with Wang's model [67]. The results showed high correlation between mean opinions score (MOS) and the predicted model results (Fig. 5). Finally, for better assessment, both the proposed method and the other noise reduction filters were applied on two different kinds of data sets of standard images from [68–70] as shown in Tables 6–8. The results exhibited better performance of the proposed method compared to the other filters for noise

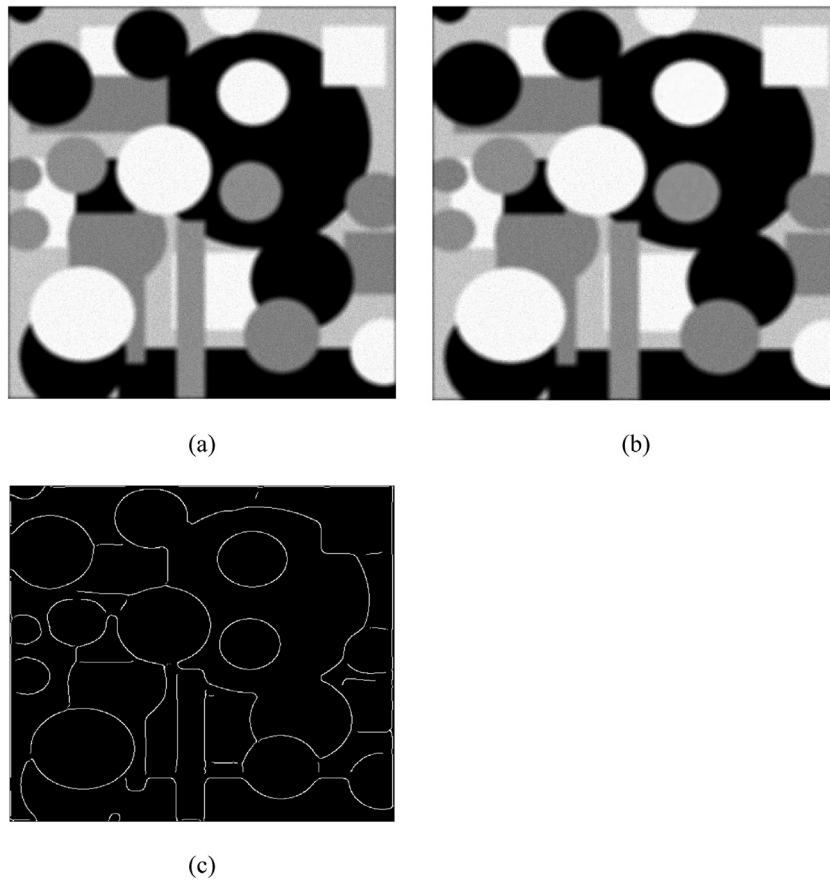


Fig. 2 – Results of proposed method and Canny edge detection for a sample of the simulation images: (a) without filter; (b) with filter; (c) with edge detection.

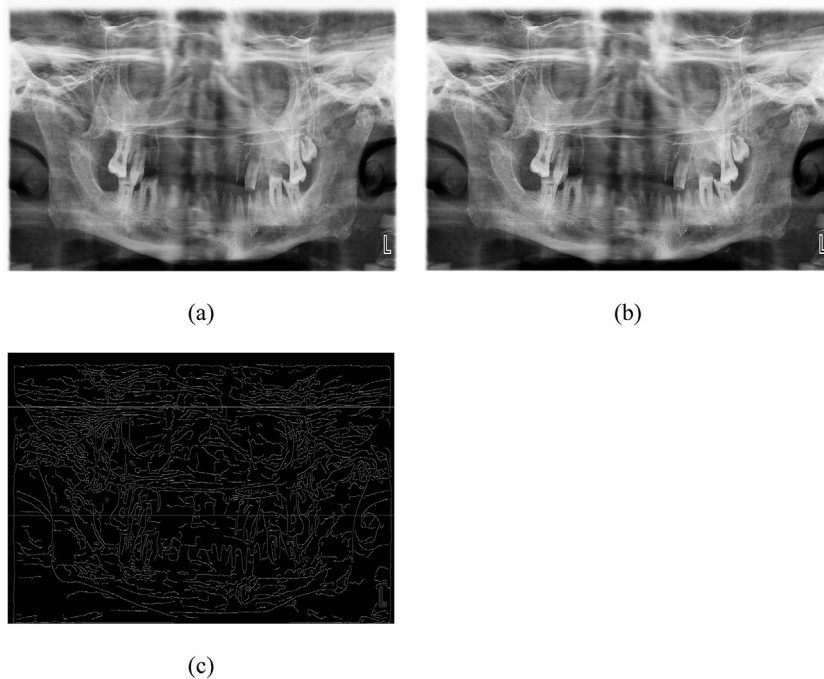


Fig. 3 – Results of proposed method and Canny edge detection for a sample of the phantom images: (a) without filter; (b) with filter; (c) with edge detection.

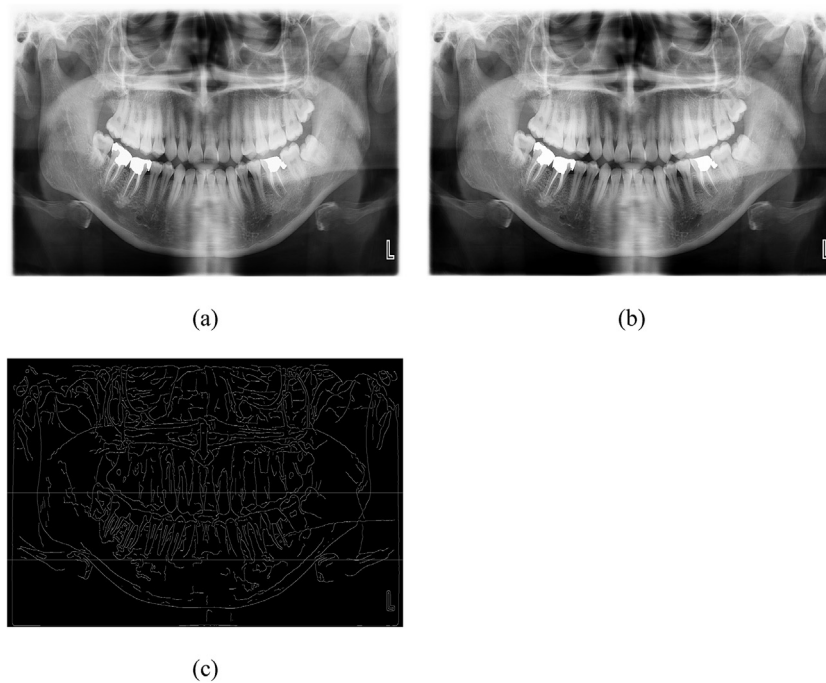


Fig. 4 – Results of proposed filter and Canny edge detection for a sample of the real images: (a) without filter; (b) with filter; (c) with edge detection.

reduction on the standard images. Since continuous superior and inferior borders of the cortex and its thickness as well as the mental foramen site are important landmarks for evaluating mandible bone so that they help physicians and maxillofacial surgeons predict early stages of osteoporosis, block inferior alveolar nerve, and confirm stability of the jaws for teeth implantation [71,72] Our study is putting more emphasis on these aspects. Table 9 shows proper capability proposed method compared with other filters in terms of noise removal.

4. Discussion

Oral and jaw injuries can be detected in digital OPG X-ray images. But they can be occasionally missed because the images are often low in contrast and high in noise [25]. Corruption of digital OPG X-ray images is generally resulted by X-ray scattering and electrical noises. They can be patterned by Poisson distribution [25]. Therefore, reducing noise and maintaining edge details are crucial for digital X-ray imaging [73]. For this purpose, the conventional noise decreasing methods such as mean, median, wiener and so on based on Fourier transform are not performable enough for denoising. Because imaging processes are regarded as non-stationary occurrences and, moreover, these filters may also smooth the edge information [74].

Recently, nonlinear iterative denoising approaches based on the PDE variants have been introduced for removing noise while preserving edge characteristics on the X-ray images [75]. Since the 2nd-order PDE is impaired by blocky events, it is

replaced by the 4th-order PDE which has less blocky effects compared to the lower order PDE. It had some benefits such as a higher capability of dissolving the fluctuations of frequency compared to the 2nd-order PDE and owing better plans for the events of curvature in the dynamical features [76,77].

TV regularization is an important tool for noise reduction. It has the capability to retain the edges. However, since basis of TV function is first order derivation of the image intensity function, it will suffer from stair cases on the ramp surfaces of the image. This effect can be reduced using higher order regularization methods [78,79].

Wavelet-based denoising approaches are used for different image types. After Dono et al.'s study, many researchers tried to find thresholds with higher performances for image denoising. There are three main methods evaluated in this paper: the Visu, SURE and Bayes shrinks. Visu shrink is not adapted to discontinuities well in the images. SURE shrink was used as a local threshold for adapting in each level. Also, wavelet coefficients of Bayes shrink had enough capability to be summarized on images' sub-bands using a generalized Gaussian distribution. It should be mentioned that the Bayes shrink is more proper for adapting both image and noise features compared with others [36,80,81].

The FGA is one of the different kinds of algorithms which has capability to manage the PDE equations using selection proper parameters and numerical plans [82]. According to the Poisoning nature of the photon-counting event for X-ray detectors, the produced signal is a signal-dependent noise. Therefore, it is difficult to be traced from the conventional Gaussian part. In order to solve this problem, Anscombe variance-stabilizing transform (AVST) can be utilized [83,84].

Table 2 – Results of different filters and Canny edge detection on the simulation, phantom and real images for one sample (used kernel in the simulated, phantom, and real images: 23×23 ; added noise to the simulated image: 10,000).

Images Filters	Simulation	Phantom	Real
Original image			
Mean			
Median			
Weighted median			
Weiner			
Gaussian Fourier			
Ideal Fourier			
Butterworth Fourier			
Sure shrink wavelet			
Bayes shrink wavelet			
Visu shrink wavelet			
Cross validation wavelet			
2nd order PDE			
4th order PDE			
TV			
Proposed			
Complex diffusion			
SFPD			

Besides, a combined filter consisted of 4th-order PDE, TV and Bayes shrink presented which accompanied with FGA algorithm and EUIGAT. Then, its performance in noise reduction was compared with other filters in three different size of kernels; 9×9 (small), 23×23 (medium) and 41×41 (large). Undoubtedly, the size of kernel is a crucial factor in fruitful utilization of image processing. The degree of noise reduction is associated with the size of kernel which larger inhibition attained by wider kernels [2,3].

In this study, the selection of three different kinds of kernels was based on the presence of structures such as soft, bone and metal tissues with different attenuation coefficients and frequency details from low to high ranges in the oral region [50]. Edge detection is a very important factor for the human visual system. Because, capability of discriminating edges for each image may lead to the intuition of elements. Canny edge detector was applied to the panoramic images due to its benefits such as reducing the occurrence of false edge or

Table 3 – Mean and standard deviation of image quality metrics for different filters in the simulated images using three kind of kernels.

Parameter Filter	MSE	PSNR	IQI	SSIM	FOM
Mean	0.345 ± 0.076 (9 × 9)	0.349 ± 0.076 (9 × 9)	0.376 ± 0.081 (9 × 9)	0.485 ± 0.106 (9 × 9)	0.464 ± 0.111 (9 × 9) 0.423 ± 0.105
	0.416 ± 0.097 (23 × 23)	0.399 ± 0.102 (23 × 23)	0.390 ± 0.086 (23 × 23)	0.415 ± 0.101 (23 × 23)	(23 × 23) 0.440 ± 0.103
	0.394 ± 0.097 (41 × 41)	0.341 ± 0.081 (41 × 41)	0.371 ± 0.081 (41 × 41)	0.380 ± 0.077 (41 × 41)	(41 × 41)
Median	0.379 ± 0.080 (9 × 9)	0.370 ± 0.083 (9 × 9)	0.366 ± 0.075 (9 × 9)	0.499 ± 0.109 (9 × 9)	0.454 ± 0.102 (9 × 9)
	0.425 ± 0.102 (23 × 23)	0.397 ± 0.096 (23 × 23)	0.402 ± 0.080 (23 × 23)	0.390 ± 0.092 (23 × 23)	0.450 ± 0.101 (23 × 23)
	0.423 ± 0.105 (41 × 41)	0.339 ± 0.076 (41 × 41)	0.390 ± 0.077 (41 × 41)	0.388 ± 0.080 (41 × 41)	0.427 ± 0.100 (41 × 41)
Weighted median	0.370 ± 0.085 (9 × 9)	0.365 ± 0.080 (9 × 9)	0.362 ± 0.070 (9 × 9)	0.482 ± 0.101 (9 × 9)	0.454 ± 0.096 (9 × 9)
	0.407 ± 0.096 (23 × 23)	0.410 ± 0.090 (23 × 23)	0.400 ± 0.085 (23 × 23)	0.408 ± 0.090 (23 × 23)	0.432 ± 0.096 (23 × 23)
	0.422 ± 0.100 (41 × 41)	0.319 ± 0.070 (41 × 41)	0.403 ± 0.080 (41 × 41)	0.394 ± 0.079 (41 × 41)	0.429 ± 0.092 (41 × 41)
Weiner	0.355 ± 0.077 (9 × 9)	0.361 ± 0.070 (9 × 9)	0.362 ± 0.074 (9 × 9)	0.468 ± 0.100 (9 × 9)	0.437 ± 0.085 (9 × 9)
	0.387 ± 0.084 (23 × 23)	0.395 ± 0.080 (23 × 23)	0.377 ± 0.071 (23 × 23)	0.417 ± 0.102 (23 × 23)	0.453 ± 0.106 (23 × 23)
	0.416 ± 0.087 (41 × 41)	0.339 ± 0.081 (41 × 41)	0.381 ± 0.075 (41 × 41)	0.403 ± 0.090 (41 × 41)	0.439 ± 0.083 (41 × 41)
Gaussian Fourier	0.398 ± 0.084 (9 × 9)	0.349 ± 0.066 (9 × 9)	0.361 ± 0.078 (9 × 9)	0.483 ± 0.088 (9 × 9)	0.450 ± 0.100 (9 × 9)
	0.414 ± 0.087 (23 × 23)	0.385 ± 0.070 (23 × 23)	0.389 ± 0.087 (23 × 23)	0.397 ± 0.087 (23 × 23)	0.436 ± 0.096 (23 × 23)
	0.393 ± 0.090 (41 × 41)	0.342 ± 0.067 (41 × 41)	0.375 ± 0.071 (41 × 41)	0.414 ± 0.087 (41 × 41)	0.429 ± 0.089 (41 × 41)
Ideal Fourier	0.390 ± 0.080 (9 × 9)	0.340 ± 0.071 (9 × 9)	0.370 ± 0.083 (9 × 9)	0.490 ± 0.096 (9 × 9)	0.427 ± 0.082 (9 × 9)
	0.395 ± 0.091 (23 × 23)	0.384 ± 0.076 (23 × 23)	0.400 ± 0.080 (23 × 23)	0.413 ± 0.080 (23 × 23)	0.420 ± 0.084 (23 × 23)
	0.409 ± 0.076 (41 × 41)	0.333 ± 0.059 (41 × 41)	0.394 ± 0.084 (41 × 41)	0.418 ± 0.096 (41 × 41)	0.443 ± 0.080 (41 × 41)
Butterworth Fourier	0.354 ± 0.072 (9 × 9)	0.367 ± 0.080 (9 × 9)	0.339 ± 0.071 (9 × 9)	0.482 ± 0.105 (9 × 9)	0.448 ± 0.087 (9 × 9)
	0.397 ± 0.081 (23 × 23)	0.390 ± 0.084 (23 × 23)	0.388 ± 0.075 (23 × 23)	0.388 ± 0.084 (23 × 23)	0.434 ± 0.091 (23 × 23)
	0.434 ± 0.091 (41 × 41)	0.343 ± 0.069 (41 × 41)	0.366 ± 0.067 (41 × 41)	0.404 ± 0.087 (41 × 41)	0.419 ± 0.094 (41 × 41)
SURE shrink wavelet	0.381 ± 0.078 (9 × 9)	0.371 ± 0.067 (9 × 9)	0.364 ± 0.070 (9 × 9)	0.460 ± 0.105 (9 × 9)	0.442 ± 0.099 (9 × 9)
	0.385 ± 0.093 (23 × 23)	0.392 ± 0.085 (23 × 23)	0.405 ± 0.085 (23 × 23)	0.406 ± 0.091 (23 × 23)	0.430 ± 0.091 (23 × 23)
	0.393 ± 0.084 (41 × 41)	0.361 ± 0.078 (41 × 41)	0.380 ± 0.074 (41 × 41)	0.404 ± 0.073 (41 × 41)	0.413 ± 0.077 (41 × 41)
Bayes shrink wavelet	0.353 ± 0.065 (9 × 9)	0.377 ± 0.063 (9 × 9)	0.369 ± 0.060 (9 × 9)	0.473 ± 0.078 (9 × 9)	0.469 ± 0.078 (9 × 9)
	0.431 ± 0.078 (23 × 23)	0.401 ± 0.069 (23 × 23)	0.397 ± 0.069 (23 × 23)	0.405 ± 0.070 (23 × 23)	0.411 ± 0.073 (23 × 23)
	0.404 ± 0.071 (41 × 41)	0.375 ± 0.060 (41 × 41)	0.366 ± 0.060 (41 × 41)	0.425 ± 0.069 (41 × 41)	0.416 ± 0.069 (41 × 41)
Visu shrink wavelet	0.366 ± 0.070 (9 × 9)	0.335 ± 0.067 (9 × 9)	0.358 ± 0.075 (9 × 9)	0.484 ± 0.101 (9 × 9)	0.431 ± 0.092 (9 × 9)
	0.386 ± 0.088 (23 × 23)	0.410 ± 0.101 (23 × 23)	0.398 ± 0.091 (23 × 23)	0.401 ± 0.095 (23 × 23)	0.439 ± 0.105 (23 × 23)
	0.407 ± 0.091 (41 × 41)	0.350 ± 0.076 (41 × 41)	0.395 ± 0.086 (41 × 41)	0.403 ± 0.085 (41 × 41)	0.416 ± 0.098 (41 × 41)

Table 3 (Continued)

Parameter Filter	MSE	PSNR	IQI	SSIM	FOM
Cross validation wavelet	0.379 ± 0.074 (9 × 9)	0.350 ± 0.076 (9 × 9)	0.351 ± 0.074 (9 × 9)	0.492 ± 0.098 (9 × 9)	0.449 ± 0.102 (9 × 9)
	0.409 ± 0.102 (23 × 23)	0.383 ± 0.087 (23 × 23)	0.390 ± 0.085 (23 × 23)	0.381 ± 0.073 (23 × 23)	0.433 ± 0.086 (23 × 23)
	0.428 ± 0.087 (41 × 41)	0.345 ± 0.069 (41 × 41)	0.382 ± 0.075 (41 × 41)	0.384 ± 0.074 (41 × 41)	0.415 ± 0.088 (41 × 41)
2nd order PDE	0.377 ± 0.065 (9 × 9)	0.366 ± 0.060 (9 × 9)	0.371 ± 0.064 (9 × 9)	0.481 ± 0.081 (9 × 9)	0.450 ± 0.083 (9 × 9)
	0.398 ± 0.068 (23 × 23)	0.406 ± 0.069 (23 × 23)	0.372 ± 0.061 (23 × 23)	0.414 ± 0.072 (23 × 23)	0.428 ± 0.068 (23 × 23)
	0.414 ± 0.070 (41 × 41)	0.338 ± 0.074 (41 × 41)	0.374 ± 0.063 (41 × 41)	0.396 ± 0.063 (41 × 41)	0.428 ± 0.068 (41 × 41)
4th order PDE	0.314 ± 0.039 (9 × 9)	0.403 ± 0.046 (9 × 9)	0.434 ± 0.046 (9 × 9)	0.542 ± 0.060 (9 × 9)	0.486 ± 0.061 (9 × 9)
	0.379 ± 0.057 (23 × 23)	0.426 ± 0.053 (23 × 23)	0.452 ± 0.057 (23 × 23)	0.433 ± 0.056 (23 × 23)	0.453 ± 0.059 (23 × 23)
	0.381 ± 0.063 (41 × 41)	0.388 ± 0.051 (41 × 41)	0.407 ± 0.053 (41 × 41)	0.430 ± 0.056 (41 × 41)	0.451 ± 0.060 (41 × 41)
TV	0.317 ± 0.040 (9 × 9)	0.395 ± 0.044 (9 × 9)	0.394 ± 0.040 (9 × 9)	0.530 ± 0.057 (9 × 9)	0.499 ± 0.060 (9 × 9)
	0.375 ± 0.060 (23 × 23)	0.429 ± 0.052 (23 × 23)	0.456 ± 0.053 (23 × 23)	0.435 ± 0.050 (23 × 23)	0.460 ± 0.060 (23 × 23)
	0.386 ± 0.060 (41 × 41)	0.390 ± 0.049 (41 × 41)	0.410 ± 0.049 (41 × 41)	0.434 ± 0.054 (41 × 41)	0.457 ± 0.057 (41 × 41)
Proposed method	0.213 ± 0.012 (9 × 9)	0.545 ± 0.073 (9 × 9)	0.554 ± 0.068 (9 × 9)	0.562 ± 0.063 (9 × 9)	0.537 ± 0.065 (9 × 9)
	0.217 ± 0.015 (23 × 23)	0.580 ± 0.069 (23 × 23)	0.579 ± 0.068 (23 × 23)	0.584 ± 0.077 (23 × 23)	0.617 ± 0.079 (23 × 23)
	0.231 ± 0.014 (41 × 41)	0.524 ± 0.079 (41 × 41)	0.571 ± 0.078 (41 × 41)	0.586 ± 0.073 (41 × 41)	0.607 ± 0.076 (41 × 41)
Complex diffusion	0.367 ± 0.080 (9 × 9)	0.338 ± 0.070 (9 × 9)	0.365 ± 0.070 (9 × 9)	0.480 ± 0.092 (9 × 9)	0.450 ± 0.094 (9 × 9)
	0.402 ± 0.095 (23 × 23)	0.409 ± 0.093 (23 × 23)	0.384 ± 0.087 (23 × 23)	0.400 ± 0.090 (23 × 23)	0.429 ± 0.100 (23 × 23)
	0.438 ± 0.085 (41 × 41)	0.322 ± 0.070 (41 × 41)	0.396 ± 0.080 (41 × 41)	0.406 ± 0.090 (41 × 41)	0.413 ± 0.094 (41 × 41)
SFPD	0.394 ± 0.084 (9 × 9)	0.355 ± 0.073 (9 × 9)	0.377 ± 0.081 (9 × 9)	0.461 ± 0.094 (9 × 9)	0.462 ± 0.089 (9 × 9)
	0.409 ± 0.090 (23 × 23)	0.402 ± 0.088 (23 × 23)	0.396 ± 0.080 (23 × 23)	0.389 ± 0.082 (23 × 23)	0.416 ± 0.097 (23 × 23)
	0.420 ± 0.088 (41 × 41)	0.354 ± 0.073 (41 × 41)	0.381 ± 0.079 (41 × 41)	0.386 ± 0.085 (41 × 41)	0.417 ± 0.096 (41 × 41)

Table 4 – Mean and Standard deviation of image quality metrics for different filters in the phantom images using three kind of kernels.

Parameter Filter	MSE	PSNR	IQI	SSIM	FOM
Mean	0.508 ± 0.068 (9 × 9)	0.459 ± 0.068 (9 × 9)	0.458 ± 0.070 (9 × 9)	0.466 ± 0.070 (9 × 9)	0.422 ± 0.055 (9 × 9)
	0.444 ± 0.064 (23 × 23)	0.516 ± 0.076 (23 × 23)	0.529 ± 0.073 (23 × 23)	0.474 ± 0.068 (23 × 23)	0.490 ± 0.070 (23 × 23)
	0.448 ± 0.067 (41 × 41)	0.485 ± 0.068 (41 × 41)	0.412 ± 0.055 (41 × 41)	0.372 ± 0.058 (41 × 41)	0.425 ± 0.060 (41 × 41)
	0.524 ± 0.071 (9 × 9)	0.523 ± 0.077 (9 × 9)	0.423 ± 0.062 (9 × 9)	0.498 ± 0.076 (9 × 9)	0.468 ± 0.064 (9 × 9)
Median	0.455 ± 0.068 (23 × 23)	0.533 ± 0.079 (23 × 23)	0.532 ± 0.077 (23 × 23)	0.469 ± 0.064 (23 × 23)	0.461 ± 0.066 (23 × 23)
	0.494 ± 0.071 (41 × 41)	0.485 ± 0.066 (41 × 41)	0.424 ± 0.059 (41 × 41)	0.384 ± 0.054 (41 × 41)	0.415 ± 0.055 (41 × 41)

Table 4 (Continued)

Parameter Filter	MSE	PSNR	IQI	SSIM	FOM
Weighted median	0.513 ± 0.070 (9 × 9)	0.473 ± 0.065 (9 × 9)	0.506 ± 0.066 (9 × 9)	0.504 ± 0.072 (9 × 9)	0.497 ± 0.068 (9 × 9)
	0.474 ± 0.069 (23 × 23)	0.510 ± 0.071 (23 × 23)	0.536 ± 0.073 (23 × 23)	0.469 ± 0.068 (23 × 23)	0.436 ± 0.060 (23 × 23)
	0.473 ± 0.063 (41 × 41)	0.470 ± 0.068 (41 × 41)	0.437 ± 0.063 (41 × 41)	0.384 ± 0.050 (41 × 41)	0.435 ± 0.059 (41 × 41)
Weiner	0.491 ± 0.068 (9 × 9)	0.466 ± 0.061 (9 × 9)	0.517 ± 0.078 (9 × 9)	0.538 ± 0.081 (9 × 9)	0.526 ± 0.073 (9 × 9)
	0.471 ± 0.066 (23 × 23)	0.504 ± 0.066 (23 × 23)	0.521 ± 0.071 (23 × 23)	0.456 ± 0.062 (23 × 23)	0.440 ± 0.059 (23 × 23)
	0.491 ± 0.070 (41 × 41)	0.481 ± 0.064 (41 × 41)	0.430 ± 0.060 (41 × 41)	0.359 ± 0.057 (41 × 41)	0.441 ± 0.063 (41 × 41)
Gaussian Fourier	0.513 ± 0.067 (9 × 9)	0.485 ± 0.069 (9 × 9)	0.468 ± 0.068 (9 × 9)	0.495 ± 0.073 (9 × 9)	0.512 ± 0.070 (9 × 9)
	0.452 ± 0.064 (23 × 23)	0.521 ± 0.069 (23 × 23)	0.534 ± 0.080 (23 × 23)	0.473 ± 0.069 (23 × 23)	0.441 ± 0.063 (23 × 23)
	0.518 ± 0.0081 (41 × 41)	0.462 ± 0.058 (41 × 41)	0.428 ± 0.057 (41 × 41)	0.395 ± 0.058 (41 × 41)	0.444 ± 0.060 (41 × 41)
Ideal Fourier	0.497 ± 0.073 (9 × 9)	0.475 ± 0.064 (9 × 9)	0.464 ± 0.064 (9 × 9)	0.502 ± 0.070 (9 × 9)	0.489 ± 0.066 (9 × 9)
	0.442 ± 0.060 (23 × 23)	0.513 ± 0.067 (23 × 23)	0.526 ± 0.076 (23 × 23)	0.496 ± 0.074 (23 × 23)	0.485 ± 0.066 (23 × 23)
	0.457 ± 0.065 (41 × 41)	0.459 ± 0.064 (41 × 41)	0.437 ± 0.062 (41 × 41)	0.419 ± 0.057 (41 × 41)	0.462 ± 0.067 (41 × 41)
Butterworth Fourier	0.530 ± 0.079 (9 × 9)	0.488 ± 0.070 (9 × 9)	0.476 ± 0.069 (9 × 9)	0.498 ± 0.067 (9 × 9)	0.499 ± 0.068 (9 × 9)
	0.466 ± 0.067 (23 × 23)	0.559 ± 0.074 (23 × 23)	0.547 ± 0.073 (23 × 23)	0.488 ± 0.071 (23 × 23)	0.455 ± 0.060 (23 × 23)
	0.478 ± 0.064 (41 × 41)	0.478 ± 0.068 (41 × 41)	0.442 ± 0.066 (41 × 41)	0.396 ± 0.053 (41 × 41)	0.448 ± 0.064 (41 × 41)
SURE shrink wavelet	0.502 ± 0.069 (9 × 9)	0.508 ± 0.069 (9 × 9)	0.474 ± 0.063 (9 × 9)	0.538 ± 0.068 (9 × 9)	0.515 ± 0.071 (9 × 9)
	0.455 ± 0.061 (23 × 23)	0.497 ± 0.066 (23 × 23)	0.503 ± 0.070 (23 × 23)	0.510 ± 0.071 (23 × 23)	0.479 ± 0.064 (23 × 23)
	0.482 ± 0.069 (41 × 41)	0.463 ± 0.058 (41 × 41)	0.439 ± 0.057 (41 × 41)	0.384 ± 0.055 (41 × 41)	0.426 ± 0.055 (41 × 41)
Bayes shrink wavelet	0.492 ± 0.062 (9 × 9)	0.499 ± 0.061 (9 × 9)	0.449 ± 0.059 (9 × 9)	0.518 ± 0.063 (9 × 9)	0.473 ± 0.060 (9 × 9)
	0.466 ± 0.058 (23 × 23)	0.549 ± 0.070 (23 × 23)	0.3543 ± 0.069 (23 × 23)	0.485 ± 0.063 (23 × 23)	0.466 ± 0.059 (23 × 23)
	0.486 ± 0.063 (41 × 41)	0.458 ± 0.051 (41 × 41)	0.402 ± 0.051 (41 × 41)	0.395 ± 0.050 (41 × 41)	0.413 ± 0.050 (41 × 41)
Visu shrink wavelet	0.481 ± 0.065 (9 × 9)	0.454 ± 0.062 (9 × 9)	0.495 ± 0.069 (9 × 9)	0.508 ± 0.074 (9 × 9)	0.488 ± 0.064 (9 × 9)
	0.463 ± 0.067 (23 × 23)	0.507 ± 0.069 (23 × 23) 0.472 ± 0.070	0.537 ± 0.073 (23 × 23)	0.501 ± 0.069 (23 × 23)	0.459 ± 0.062 (23 × 23)
	0.493 ± 0.068 (41 × 41)	0.472 ± 0.070 (41 × 41)	0.447 ± 0.064 (41 × 41)	0.414 ± 0.057 (41 × 41)	0.448 ± 0.062 (41 × 41)
Cross validation wavelet	0.565 ± 0.076 (9 × 9)	0.485 ± 0.067 (9 × 9)	0.480 ± 0.067 (9 × 9)	0.480 ± 0.069 (9 × 9)	0.484 ± 0.067 (9 × 9) 0.451 ± 0.060
	0.451 ± 0.061 (23 × 23)	0.575 ± 0.073 (23 × 23)	0.540 ± 0.074 (23 × 23)	0.466 ± 0.067 (23 × 23)	(23 × 23) 0.434 ± 0.060
	0.484 ± 0.066 (41 × 41)	0.439 ± 0.055 (41 × 41)	0.416 ± 0.057 (41 × 41)	0.409 ± 0.054 (41 × 41)	(41 × 41)
2nd order PDE	0.555 ± 0.068 (9 × 9)	0.490 ± 0.060 (9 × 9)	0.462 ± 0.058 (9 × 9)	0.505 ± 0.061 (9 × 9)	0.502 ± 0.063 (9 × 9)
	0.455 ± 0.058 (23 × 23)	0.524 ± 0.062 (23 × 23)	0.519 ± 0.059 (23 × 23)	0.482 ± 0.059 (23 × 23)	0.452 ± 0.056 (23 × 23)
	0.499 ± 0.061 (41 × 41)	0.485 ± 0.057 (41 × 41)	0.436 ± 0.053 (41 × 41)	0.375 ± 0.048 (41 × 41)	0.412 ± 0.050 (41 × 41)

Table 4 (Continued)

Parameter Filter	MSE	PSNR	IQI	SSIM	FOM
4th order PDE	0.468 ± 0.058 (9 × 9)	0.549 ± 0.056 (9 × 9)	0.522 ± 0.054 (9 × 9)	0.546 ± 0.064 (9 × 9)	0.544 ± 0.063 (9 × 9)
	0.418 ± 0.047 (23 × 23)	0.564 ± 0.061 (23 × 23)	0.565 ± 0.065 (23 × 23) 0.460 ± 0.054	0.511 ± 0.058 (23 × 23)	0.509 ± 0.051 (23 × 23)
	0.435 ± 0.050 (41 × 41)	0.493 ± 0.058 (41 × 41)	(41 × 41)	0.428 ± 0.050 (41 × 41)	0.455 ± 0.054 (41 × 41)
TV	0.460 ± 0.054 (9 × 9)	0.555 ± 0.058 (9 × 9)	0.528 ± 0.053 (9 × 9)	0.554 ± 0.066 (9 × 9)	0.553 ± 0.067 (9 × 9)
	0.400 ± 0.044 (23 × 23)	0.570 ± 0.059 (23 × 23)	0.578 ± 0.061 (23 × 23)	0.517 ± 0.054 (23 × 23)	0.516 ± 0.055 (23 × 23)
	0.423 ± 0.044 (41 × 41)	0.506 ± 0.052 (41 × 41)	0.472 ± 0.050 (41 × 41)	0.437 ± 0.046 (41 × 41)	0.467 ± 0.048 (41 × 41)
Proposed	0.337 ± 0.023 (9 × 9)	0.661 ± 0.076 (9 × 9)	0.660 ± 0.072 (9 × 9)	0.693 ± 0.081 (9 × 9)	0.664 ± 0.082 (9 × 9)
	0.301 ± 0.0199 (23 × 23)	0.681 ± 0.076 (23 × 23)	0.686 ± 0.079 (23 × 23)	0.634 ± 0.074 (23 × 23)	0.618 ± 0.070 (23 × 23)
	0.363 ± 0.027 (41 × 41)	0.578 ± 0.068 (41 × 41)	0.538 ± 0.064 (41 × 41)	0.502 ± 0.061 (41 × 41)	0.541 ± 0.065 (41 × 41)
Complex diffusion	0.467 ± 0.061 (9 × 9)	0.491 ± 0.066 (9 × 9)	0.481 ± 0.064 (9 × 9)	0.495 ± 0.074 (9 × 9)	0.471 ± 0.063 (9 × 9)
	0.460 ± 0.061 (23 × 23)	0.547 ± 0.072 (23 × 23)	0.503 ± 0.070 (23 × 23)	0.467 ± 0.062 (23 × 23)	0.430 ± 0.056 (23 × 23)
	0.480 ± 0.063 (41 × 41)	0.481 ± 0.068 (41 × 41)	0.420 ± 0.055 (41 × 41)	0.361 ± 0.047 (41 × 41)	0.422 ± 0.055 (41 × 41)
SFPD	0.537 ± 0.071 (9 × 9)	0.482 ± 0.069 (9 × 9)	0.502 ± 0.070 (9 × 9)	0.502 ± 0.070 (9 × 9)	0.490 ± 0.070 (9 × 9)
	0.428 ± 0.060 (23 × 23)	0.529 ± 0.076 (23 × 23)	0.510 ± 0.074 (23 × 23)	0.490 ± 0.070 (23 × 23)	0.462 ± 0.061 (23 × 23)
	0.511 ± 0.071 (41 × 41)	0.461 ± 0.063 (41 × 41)	0.442 ± 0.059 (41 × 41)	0.382 ± 0.051 (41 × 41)	0.442 ± 0.058 (41 × 41)

Table 5 – Mean and Standard deviation of image quality metrics for different filters in the real images using three kind of kernels.

Parameter Filter	MSE	PSNR	IQI	SSIM	FOM
Mean	0.447 ± 0.065 (9 × 9)	0.520 ± 0.071 (9 × 9)	0.492 ± 0.072 (9 × 9)	0.486 ± 0.070 (9 × 9)	0.519 ± 0.068 (9 × 9)
	0.467 ± 0.062 (23 × 23)	0.486 ± 0.064 (23 × 23)	0.456 ± 0.065 (23 × 23)	0.498 ± 0.070 (23 × 23)	0.423 ± 0.060 (23 × 23)
	0.483 ± 0.069 (41 × 41)	0.541 ± 0.076 (41 × 41)	0.484 ± 0.070 (41 × 41)	0.476 ± 0.071 (41 × 41)	0.461 ± 0.068 (41 × 41)
Median	0.465 ± 0.070 (9 × 9)	0.509 ± 0.066 (9 × 9)	0.481 ± 0.063 (9 × 9)	0.481 ± 0.065 (9 × 9)	0.494 ± 0.063 (9 × 9)
	0.458 ± 0.060 (23 × 23)	0.494 ± 0.067 (23 × 23)	0.422 ± 0.060 (23 × 23)	0.510 ± 0.073 (23 × 23)	0.426 ± 0.056 (23 × 23)
	0.497 ± 0.072 (41 × 41)	0.531 ± 0.071 (41 × 41)	0.473 ± 0.068 (41 × 41)	0.509 ± 0.067 (41 × 41)	0.461 ± 0.063 (41 × 41)
Weighted median	0.405 ± 0.059 (9 × 9)	0.513 ± 0.070 (9 × 9)	0.492 ± 0.067 (9 × 9)	0.474 ± 0.062 (9 × 9)	0.497 ± 0.067 (9 × 9)
	0.453 ± 0.062 (23 × 23)	0.495 ± 0.067 (23 × 23)	0.436 ± 0.063 (23 × 23)	0.538 ± 0.074 (23 × 23)	0.438 ± 0.059 (23 × 23)
	0.497 ± 0.067 (41 × 41)	0.530 ± 0.074 (41 × 41)	0.469 ± 0.064 (41 × 41)	0.490 ± 0.068 (41 × 41)	0.463 ± 0.065 (41 × 41)
Weiner	0.427 ± 0.056 (9 × 9)	0.538 ± 0.076 (9 × 9)	0.487 ± 0.065 (9 × 9)	0.476 ± 0.070 (9 × 9)	0.514 ± 0.070 (9 × 9)
	0.456 ± 0.067 (23 × 23)	0.492 ± 0.070 (23 × 23)	0.433 ± 0.064 (23 × 23)	0.488 ± 0.069 (23 × 23)	0.407 ± 0.060 (23 × 23)
	0.506 ± 0.068 (41 × 41)	0.546 ± 0.074 (41 × 41)	0.467 ± 0.061 (41 × 41)	0.488 ± 0.064 (41 × 41)	0.455 ± 0.061 (41 × 41)

Table 5 (Continued)

Parameter Filter	MSE	PSNR	IQI	SSIM	FOM
Gaussian Fourier	0.439 ± 0.060 (9 × 9)	0.513 ± 0.073 (9 × 9)	0.499 ± 0.073 (9 × 9)	0.453 ± 0.064 (9 × 9)	0.498 ± 0.074 (9 × 9)
	0.429 ± 0.060 (23 × 23)	0.513 ± 0.075 (23 × 23)	0.440 ± 0.063 (23 × 23)	0.531 ± 0.075 (23 × 23)	0.454 ± 0.062 (23 × 23)
	0.515 ± 0.0076 (41 × 41)	0.524 ± 0.070 (41 × 41)	0.461 ± 0.063 (41 × 41)	0.491 ± 0.071 (41 × 41)	0.438 ± 0.059 (41 × 41)
Ideal Fourier	0.452 ± 0.064 (9 × 9)	0.506 ± 0.066 (9 × 9)	0.495 ± 0.070 (9 × 9)	0.470 ± 0.068 (9 × 9)	0.495 ± 0.068 (9 × 9)
	0.456 ± 0.065 (23 × 23)	0.486 ± 0.069 (23 × 23)	0.434 ± 0.060 (23 × 23)	0.508 ± 0.070 (23 × 23)	0.425 ± 0.057 (23 × 23)
	0.497 ± 0.074 (41 × 41)	0.529 ± 0.071 (41 × 41)	0.448 ± 0.065 (41 × 41)	0.497 ± 0.066 (41 × 41)	0.444 ± 0.058 (41 × 41)
Butterworth Fourier	0.406 ± 0.055 (9 × 9)	0.490 ± 0.071 (9 × 9)	0.485 ± 0.069 (9 × 9)	0.467 ± 0.061 (9 × 9)	0.467 ± 0.067 (9 × 9)
	0.430 ± 0.059 (23 × 23)	0.466 ± 0.064 (23 × 23)	0.437 ± 0.059 (23 × 23)	0.513 ± 0.076 (23 × 23)	0.415 ± 0.058 (23 × 23)
	0.500 ± 0.073 (41 × 41)	0.562 ± 0.076 (41 × 41)	0.478 ± 0.064 (41 × 41)	0.480 ± 0.065 (41 × 41)	0.441 ± 0.063 (41 × 41)
SURE shrink wavelet	0.454 ± 0.063 (9 × 9)	0.517 ± 0.070 (9 × 9)	0.471 ± 0.062 (9 × 9)	0.498 ± 0.068 (9 × 9)	0.529 ± 0.069 (9 × 9)
	0.414 ± 0.054 (23 × 23)	0.474 ± 0.064 (23 × 23)	0.456 ± 0.060 (23 × 23)	0.527 ± 0.073 (23 × 23)	0.422 ± 0.057 (23 × 23)
	0.500 ± 0.065 (41 × 41)	0.536 ± 0.070 (41 × 41)	0.474 ± 0.066 (41 × 41)	0.474 ± 0.063 (41 × 41)	0.459 ± 0.060 (41 × 41)
Bayes shrink wavelet	0.425 ± 0.054 (9 × 9)	0.502 ± 0.062 (9 × 9)	0.504 ± 0.065 (9 × 9)	0.486 ± 0.059 (9 × 9)	0.491 ± 0.062 (9 × 9)
	0.449 ± 0.056 (23 × 23)	0.497 ± 0.060 (23 × 23)	0.450 ± 0.057 (23 × 23)	0.533 ± 0.066 (23 × 23)	0.428 ± 0.054 (23 × 23)
	0.521 ± 0.063 (41 × 41)	0.543 ± 0.066 (41 × 41)	0.459 ± 0.058 (41 × 41)	0.477 ± 0.062 (41 × 41)	0.434 ± 0.056 (41 × 41)
Visu shrink wavelet	0.440 ± 0.061 (9 × 9)	0.531 ± 0.075 (9 × 9)	0.488 ± 0.073 (9 × 9)	0.469 ± 0.070 (9 × 9)	0.486 ± 0.072 (9 × 9)
	0.443 ± 0.058 (23 × 23)	0.487 ± 0.065 (23 × 23) 0.538 ± 0.071	0.439 ± 0.060 (23 × 23)	0.507 ± 0.066 (23 × 23)	0.448 ± 0.059 (23 × 23)
	0.505 ± 0.068 (41 × 41)	(41 × 41)	0.457 ± 0.063 (41 × 41)	0.484 ± 0.067 (41 × 41)	0.453 ± 0.060 (41 × 41)
Cross validation wavelet	0.453 ± 0.060 (9 × 9)	0.516 ± 0.067 (9 × 9)	0.490 ± 0.060 (9 × 9)	0.482 ± 0.064 (9 × 9)	0.481 ± 0.067 (9 × 9)
	0.435 ± 0.060 (23 × 23)	0.448 ± 0.056 (23 × 23)	0.456 ± 0.063 (23 × 23)	0.526 ± 0.070 (23 × 23)	0.447 ± 0.060 (23 × 23)
	0.479 ± 0.064 (41 × 41)	0.544 ± 0.073 (41 × 41)	0.474 ± 0.063 (41 × 41)	0.478 ± 0.064 (41 × 41)	0.461 ± 0.062 (41 × 41)
2nd order PDE	0.441 ± 0.054 (9 × 9)	0.508 ± 0.065 (9 × 9)	0.492 ± 0.057 (9 × 9)	0.478 ± 0.056 (9 × 9)	0.514 ± 0.070 (9 × 9)
	0.437 ± 0.049 (23 × 23)	0.456 ± 0.058 (23 × 23)	0.463 ± 0.060 (23 × 23)	0.538 ± 0.062 (23 × 23)	0.444 ± 0.056 (23 × 23)
	0.500 ± 0.062 (41 × 41)	0.533 ± 0.066 (41 × 41)	0.489 ± 0.056 (41 × 41)	0.492 ± 0.060 (41 × 41)	0.438 ± 0.054 (41 × 41)
4th order PDE	0.390 ± 0.045 (9 × 9)	0.545 ± 0.060 (9 × 9)	0.512 ± 0.060 (9 × 9)	0.509 ± 0.057 (9 × 9)	0.528 ± 0.060 (9 × 9)
	0.403 ± 0.043 (23 × 23)	0.523 ± 0.060 (23 × 23)	0.485 ± 0.055 (23 × 23) 0.495 ± 0.059	0.561 ± 0.066 (23 × 23)	0.467 ± 0.056 (23 × 23)
	0.464 ± 0.054 (41 × 41)	0.584 ± 0.065 (41 × 41)	(41 × 41)	0.520 ± 0.059 (41 × 41)	0.478 ± 0.055 (41 × 41)
TV	0.377 ± 0.040 (9 × 9)	0.556 ± 0.056 (9 × 9)	0.521 ± 0.056 (9 × 9)	0.517 ± 0.053 (9 × 9)	0.537 ± 0.056 (9 × 9)
	0.386 ± 0.040 (23 × 23)	0.532 ± 0.057 (23 × 23)	0.508 ± 0.059 (23 × 23)	0.588 ± 0.063 (23 × 23)	0.481 ± 0.052 (23 × 23)
	0.449 ± 0.050 (41 × 41)	0.597 ± 0.062 (41 × 41)	0.507 ± 0.053 (41 × 41)	0.532 ± 0.062 (41 × 41)	0.491 ± 0.058 (41 × 41)

Table 5 (Continued)

Parameter Filter	MSE	PSNR	IQI	SSIM	FOM
Proposed	0.350 ± 0.025 (9 × 9)	0.703 ± 0.081 (9 × 9)	0.678 ± 0.078 (9 × 9)	0.666 ± 0.079 (9 × 9)	0.687 ± 0.079 (9 × 9)
	0.296 ± 0.020 (23 × 23)	0.632 ± 0.081 (23 × 23)	0.599 ± 0.075 (23 × 23)	0.667 ± 0.080 (23 × 23)	0.591 ± 0.075 (23 × 23)
	0.370 ± 0.027 (41 × 41)	0.665 ± 0.079 (41 × 41)	0.605 ± 0.072 (41 × 41)	0.617 ± 0.073 (41 × 41)	0.620 ± 0.075 (41 × 41)
Complex diffusion	0.437 ± 0.058 (9 × 9)	0.527 ± 0.071 (9 × 9)	0.499 ± 0.068 (9 × 9)	0.496 ± 0.067 (9 × 9)	0.494 ± 0.068 (9 × 9)
	0.468 ± 0.062 (23 × 23)	0.463 ± 0.063 (23 × 23)	0.448 ± 0.062 (23 × 23)	0.512 ± 0.068 (23 × 23)	0.444 ± 0.061 (23 × 23)
	0.499 ± 0.065 (41 × 41)	0.545 ± 0.075 (41 × 41)	0.491 ± 0.067 (41 × 41)	0.503 ± 0.069 (41 × 41)	0.454 ± 0.062 (41 × 41)
SFPD	0.431 ± 0.057 (9 × 9)	0.518 ± 0.076 (9 × 9)	0.502 ± 0.075 (9 × 9)	0.470 ± 0.063 (9 × 9)	0.492 ± 0.065 (9 × 9)
	0.442 ± 0.052 (23 × 23)	0.475 ± 0.067 (23 × 23)	0.438 ± 0.058 (23 × 23)	0.510 ± 0.073 (23 × 23)	0.418 ± 0.057 (23 × 23)
	0.512 ± 0.071 (41 × 41)	0.523 ± 0.078 (41 × 41)	0.472 ± 0.070 (41 × 41)	0.505 ± 0.072 (41 × 41)	0.464 ± 0.066 (41 × 41)

lesion real edge creation. Besides, it inhibits several responses to real edges compared to other edge detection methods [60,85]. Experimental results showed the proposed filter combined with Canny edge detection is better than other filters at noise suppression with respect to MSE, PSNR, IQI, SSIM and FOM criteria. Frosio et al. suggested TV regularization and wavelet decomposition for denoising X-ray images degraded based on Poisson noise considering statistical properties of Poisson noises and detecting procedure of photons by sensors [50]. The present study was in agreement with this investigation.

Among researches about Poisson noise removal methods, studies by Deledalle et al. and Makitalo et al. should be mentioned which suffered from high execution time or great complexity [14,86]. Also, some researches were done for Poisson noise reduction using designing filters such as enhanced Bayes shrink method in wavelet domain, improved

median filter, dual tree complex wavelet transform filter and combined curvelet transform with variance stabilization [19]. This study is in agreement with previous studies and it is performable somewhere else in MSE, PSNR, IQI, SSIM and FOM criteria [18-26].

This may be resulted from the use of EUIGAT and the FGA for proposing a new approach. The EUIGAT is variance-stabilization transformation that does not have drawbacks of other inverse transforms. Because not only algebraic inverse usually leads to unwanted bias in estimation of the mean, but also the square-root transform is nonlinear and asymptotically unbiased inverse could not be appropriate for photon-limited imaging [86-88]. Also, the FGA is often recognized as a way to optimize function. It effectively locates the total solution space without computing the fitness for all of searchable points. Unlike other methods, this type of search algorithm saves FGA from being trapped by optimal local points [54,89]. Therefore, it is able to govern the PDE equations. It has to be considered that any PDE and regularization-based methods are time-consuming because of their iterations. In this study, we used Bayes shrinkage, EUIGAT and the FGA which may be proper choices for decreasing the number of iterations and managing weight coefficients.

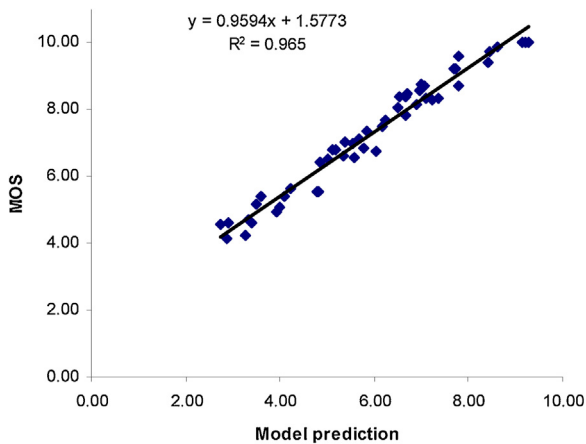


Fig. 5 – Wang's model prediction [67] results compared with (mean opinion score) MOS from the data sets of real images (used kernel in the real images: 23 × 23; and N = 104).

5. Conclusion

This paper proposed FGA-based noise removal approach which combined with Canny edge detection. Experimental results and discussion show effectiveness of the proposed method against other methods for Poisson noise removal and detail conservation of X-ray digital panoramic images. In fact, the presented approach improves physicians' and dentists' skills more to discern normal and pathological situations about the teeth, jaws, TMJ and alveolar lobes of the maxillary sinuses in face region. Also, this filter may enhance the capability of physicians for diagnosing changes of the

Table 6 - Eight standard images from two groups datasets [68,69], and three groups of datasets simulation (N = 110), phantom (N = 106), and real (N = 104) images.

Image processing images			
A1	B1	C1	D1
E1	F1	G1	H1
Cephalometric images			
I1	J1	K1	L1
M1	N1	O1	P1
Simulation images			
Q1	R1	S1	T1
U1	V1	W1	X1
Phantom images			
Y1	Z1	A2	B2
C2	D2	E2	F2
Real images			
G2	H2	I2	J2
K2	L2	M2	N2

Table 7 – Results of different filters on one sample of standard cephalometric images datasets [69] (used kernel in cephalometric image: 23×23 ; added noise to the cephalometric image: 10,000).








Image Filters	Cephalometric image
Original images	
Mean	
Median	
Weighted median	
Weiner	
Gaussian Fourier	
Ideal Fourier	

Table 7 (Continued)








Image Filters	Cephalometric image
Butterworth Fourier	
SURE shrink wavelet	
Bayes shrink wavelet	
Visu shrink wavelet	
Cross validation wavelet	
2nd order PDE	
4th order PDE	





Table 7 (Continued)	
Image Filters	Cephalometric image
TV	
Proposed	
Complex diffusion	
SFPD	






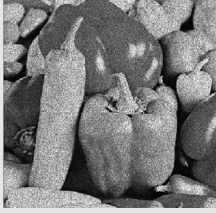
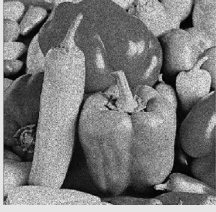
Table 8 (Continued)	
Image Filters	Peppers
Median	
Weighted median	
Weiner	
Gaussian Fourier	
Ideal Fourier	
Butterworth Fourier	
Sure shrink wavelet	

Table 8 – Results of different filters on one sample of the standard image processing datasets [68] (used kernel in standard image: 23×23 ; added noise to the standard image: 10,000).


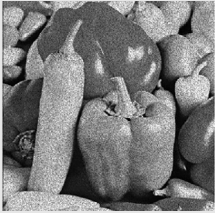
Image Filters	Peppers
Original images	
Mean	

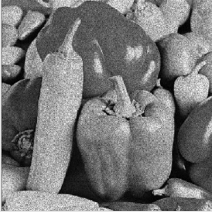
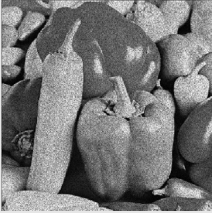
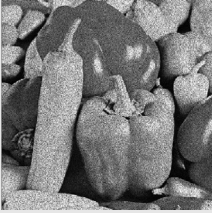
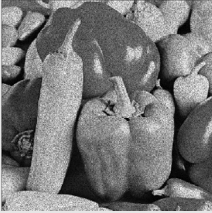
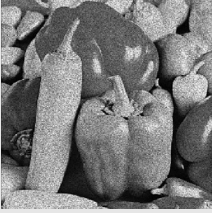
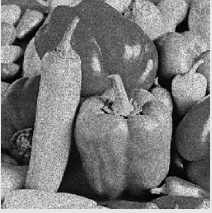
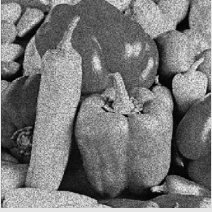
Table 8 (Continued)	
Image Filters	Peppers
Bayes shrink wavelet	
Visu shrink wavelet	
Cross validation wavelet	
2nd order PDE	
4th order PDE	
TV	
Proposed	

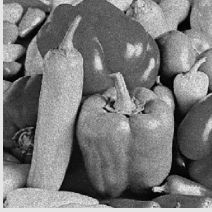
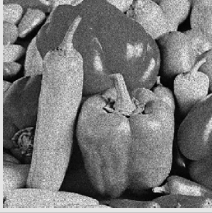
Table 8 (Continued)	
Image Filters	Peppers
Complex diffusion	
SFPD	

Table 9 – Results of different filters on the cortex and mental foramen in the mandible bone X-ray digital OPG images for one sample (used kernel in the real images: 23×23 ; $N = 104$).

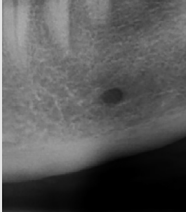
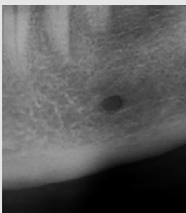
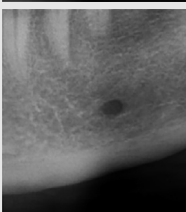
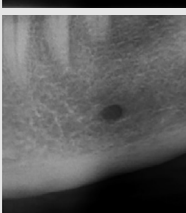
Images Filters	Cortex and mental foramen in the mandible bone
Original images	
Mean	
Median	
Weighted median	

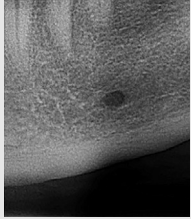
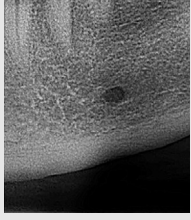
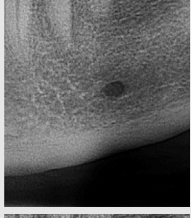
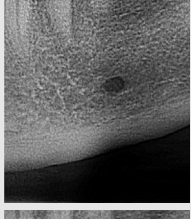
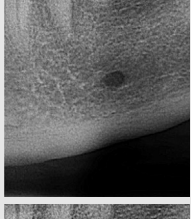
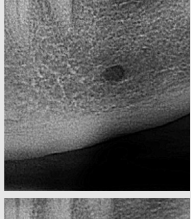
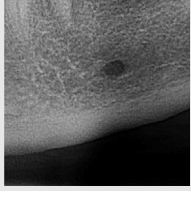
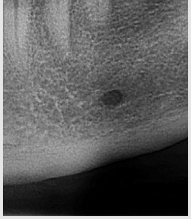
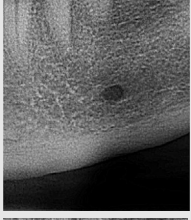
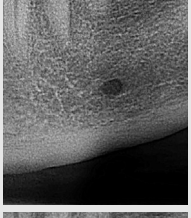
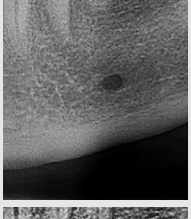
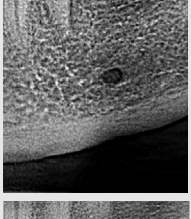
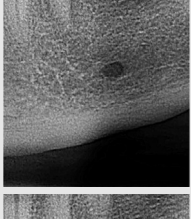
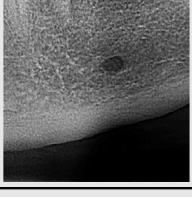
Table 9 (Continued)	
Images Filters	Cortex and mental foramen in the mandible bone
Weiner	
Gaussian Fourier	
Ideal Fourier	
Butterworth Fourier	
Sure shrink wavelet	
Bayes shrink wavelet	
Visu shrink wavelet	

Table 9 (Continued)	
Images Filters	Cortex and mental foramen in the mandible bone
Cross validation wavelet	
2nd order PDE	
4th order PDE	
TV	
Proposed	
Complex diffusion	
SFPD	

anatomical panoramic landmarks associated with osteoporosis progression in the mandible bone.

Compliance with ethical standards

Conflict of interest

The authors declare that they have no conflict of interest.

Ethical approval

All procedures performed in studies involving human participants were in accordance with the ethical standards of the institutional and/or national research committee and with the 1964 Helsinki declaration and its later amendments or comparable ethical standards. This article does not contain any studies with animals performed by any of the authors.

Informed consent

Informed consent was obtained from all individual participants included in the study.

REFERENCES

- [1] Chikhalekar AT. Analysis of image processing for digital X-ray. *Int Res Eng Technol* 2016;3:1364–8.
- [2] Yousif Abdallah YM, Almoustafa AA, Elhadi G, Mohammed M, Khalafallah O, Khalid T. Application of analysis approach in noise estimation in panoramic X-rays images using image processing program (Matlab). *Can J Med* 2011;2:38–48.
- [3] Yousif Abdallah YM, Abdelwahab RI. Improvement of orthopantography (OPG) images using texture analysis. *Int J Sci Res* 2014;3:1771–5.
- [4] Sindu YU, Ravikiran A, Swamy RR, Nayyar AS, Kartheek B. Digital panoramic radiography: an aid in the early detection of Osteoporotic signs. *Arch Med Health Sci* 2017;37:205–11.
- [5] Malhotra A, Kumar EAD. Image denoising with various filtering techniques. *Int J Adv Res Comput Sci Technol* 2015;3:129–31.
- [6] Mredula L, Dorairangaswamy MA. An extensive review of significant researches on medical image denoising technique. *Int J Comput Appl* 2013;64:1–12.
- [7] Thakur KV, Damodare OH, Sapkal AM. Poisson noise reducing bilateral filter. *Procedia Comput Sci* 2016;79:861–5.
- [8] Kumar N, Nachamai M. Noise removal and filtering techniques used in medical images. *Orient J Comput Sci Technol* 2017;10:103–13.
- [9] Das S, Saikia J, Das S, Goni N. A comparative study different noise filtering techniques in digital images. *Int J Eng Gen Sci* 2015;3:180–90.
- [10] Sutha S, Leavline EJ, Singh DAAG. A comprehensive study on wavelet based shrinkage methods for denoising natural images. *WSEAS Trans Signal Process* 2013;9:203–15.
- [11] Khosravi MH, Hassanpour H. Image denoising using anisotropic equations on reflection and illustration components of image. *Int J Eng* 2014;27:1339–48.
- [12] Figueiredo MAT, Oliveira DJP, Nowak RD. On total variation denoising: a new majorization-minimization algorithm and experimental comparison with wavelet denoising. *IEEE International Conference on Image Processing*. 2006. pp. 2633–6.
- [13] Chan TF, Osher S, Shen J. The digital TV filter and nonlinear denoising. *IEEE Trans Image Process* 2001;10:231–41.
- [14] Deledalle CA, Tupin F, Denis L. Poisson NL means: Unsupervised nonlocal means for Poisson noise. *Proceedings of 2010 IEEE 17th International Conference on Image Processing*; 2010. p. 26–9.
- [15] Dabov K, Foi A, Katkovonik V, Egiazarian K. Image denoising with block-matching and 3D filtering. *Proceedings of SPIE Electronic Imaging*, 2006:06, no. 6064A-30, San Jose, California, USA; 2006.
- [16] Makitalo M, Foi A. Optimal inversion of generalized Anscombe transform for Poisson-Gaussian noise. *IEEE Trans Image Process* 2013;22:91–103.
- [17] Wang L, Lu J, Li Y, Yahagi T, Okamoto T. Noise removal for medical X-ray images in wavelet domain. *Electr Eng Jpn* 2008;163:37–46.
- [18] Subbuthai P, Kavithabharathi K, Muruanand S. Reduction of types of noises in dental images. *Int J Comput Appl Technol Res* 2013;2:436–42.
- [19] Du L, Wen Y, Ma J. Dual tree complex wavelet transform and Bayesian estimation based denoising of Poisson-corrupted X-ray images. *Fourth International Conference on Intelligent Processing (ICICIP)*, June 9–11, 2013, Beijing, China; 2013.
- [20] Jisha JU, Sureshkumar V. Poisson noise removal in biomedical images using non-linear techniques. *Int J Adv Res Electr Electron Instrum Eng* 2014;3:131–6.
- [21] Ghaheri A, Shoar S, Naderan M, Hoseini SS. The applications of genetic algorithms in medicine. *Oman Med J* 2015;30:406–16.
- [22] Boyat AK, Joshi BK. Noise models in digital image processing. *Signal Image Process* 2015;6:63–75.
- [23] Li Y, Lu J, Wang L, Yahagi T. Noise removal for degraded images with Poisson noise using M-transformation and Bayes shrink method. *Electr Eng Jpn* 2007;90:503–12.
- [24] Vijayalakshmi A, Titus C, Lilly Beaulah H. Image denoising for different noise models by various filters: a brief survey. *Int J Emerg Trends Technol Comput Sci* 2014;3:42–5.
- [25] Thamocharan B, Menaka M, Vaidyanathan S, Ravikumar S. Survey on image processing in the field of denoising techniques edge detection techniques on radiographic images. *J Theor Appl Inf Technol* 2012;41:26–34.
- [26] Jacop RMR, Prabakar S, Porkumar K. Fetal cardiac structure detection from ultrasound sequences. *Int J Instrum Autom* 2013;2:12–6.
- [27] Deepa P, Suganthi M. Performance evaluation of various denoising filters for medical image. *Int J Comput Sci Inf Technol* 2014;5:4205–9.
- [28] Shumulevich I, Arce GR. Spectral design of weighted median filters admitting negative weights. *IEEE Signal Process Lett* 2001;8:313–6.
- [29] Soni T, Rathor N. Removal of high density impulse noise use efficient median filter for digital image. *Int J Comput Appl* 2015;115:25–31.
- [30] Sami I, Thakur A, Kumar R. Image denoising for Gaussian noise reduction in bionics using DWT technique. *Int J Electron Commun Technol* 2013;4:62–7.
- [31] Chhabra T, Dua G, Malhotra T. Comparative analysis of methods to denoise CT scan images. *Int J Adv Res Electr Electron Instrum Eng* 2013;2:3363–9.
- [32] Hafizah WM, Supriyanto E. Comparative evaluation of ultrasound kidney image enhancement techniques. *Int J Comput Appl* 2011;21:15–9.
- [33] Ojha A, Tiwari N. A study on image denoising with its techniques and types of noise. *Int J Adv Res Appl Sci Eng Technol* 2015;3:455–61.

- [34] Kumbhakarna V, Patil VR, Kawathekar S. Review on Speckle noise reduction techniques for medical ultrasound image processing. *Int J Comput Tech* 2015;2:24–7.
- [35] Rafati M, Arabfard M, Rafati Rahimzadeh M, Maghsoudloo M. Assessment of noise reduction in ultrasound of common carotid and brachial arteries. *IET Comput Vis* 2016;10:1–8.
- [36] Sulochana S, Vidhya R, Vijayasekaran D, Mohanraj K. Denoising and dimensionality reduction of hyperspectral images using framelet with different shrinkage functions. *Indian J Geo-Marine Sci* 2016;45:978–86.
- [37] Rai RK, Asnani J, Sontakke TR. Review of shrinkage techniques for image denoising. *Int J Comput Appl* 2012;42:13–6.
- [38] Sivakumar R, Gayathri MK, Nedumaran D. Speckle filtering of ultrasound B-mode images – a comparative study single scale spatial adaptive filters, multiscale filter and diffusion filters. *Int J Eng Technol* 2010;2:514–23.
- [39] Khmag A, Ramli AR, Hashim SJ, Al-Haddad SAR. Review of image denoising algorithms based on the wavelet transformation. *Int J Adv Trends Comput Sci Eng* 2013;2:1–7.
- [40] Jansen M, Uytterhoeven G, Bultheel A. Image de-noising by integer wavelet transforms and generalized cross validation. *Med Phys* 1999;26:622–30.
- [41] Geethalakshmi SN, Sugunia J. Hybrid models for denoising ultrasonic images. *J Global Res Comput Sci* 2010;1:38–45.
- [42] You YL, Kaveh M. Fourth-order partial differential equations for noise removal. *IEEE Trans Image Process* 2000;9:1723–30.
- [43] Nikpour M, Hassanpour H. Using diffusion equations for improving performance of wavelet-based image denoising techniques. *IET Image Process* 2010;4:452–62.
- [44] Khanian M, Feizi A, Davari A. An optimal partial differential equations-based stopping criterion for medical denoising. *J Med Signals Sens* 2014;4:72–83.
- [45] Nadernejad E, Koohi H, Hassanpour H. PDEs-based method for image enhancement. *Appl Math Sci* 2008;2:981–93.
- [46] Hajjaboli MR. An anisotropic fourth-order diffusion filter for image noise removal. *Int J Comput Vis* 2011;92:177–91.
- [47] Rudin LI, Osher S, Fatemi E. Nonlinear total variation based noise removal algorithms. *Physica D* 1999;60:259–68.
- [48] Zhang Y, Cheng HD, Chen Y, Huang J. A novel noise removal method based on fractional anisotropic diffusion and subpixel approach. *New Math Nat Comput* 2011;1:173–85.
- [49] Kittisuwan P. Medical image denoising using simple form of MMSE estimation in Poisson-Gaussian noise model. *Int J Biomath* 2016;9:1–9. <http://dx.doi.org/10.1142/S1793524516500200>
- [50] Frasio I, Oliveira C, Lucchese M, Borghese NA, Boccacci P. Bayesian denoising in digital radiography: a comparison in the dental field. *Comput Med Imaging Graph* 2013;37:28–39.
- [51] Al Shalabi L, Shaaban Z, Kasasbeh B. Data mining: a preprocessing engine. *J Comput Sci* 2006;9:735–9.
- [52] Rosenfeld A, Pealtz JL. Sequential operations in digital picture processing. *J Assoc Comput Mach* 1966;13:471–97.
- [53] Darmanayagam SE, Harichandran KN, Cyril SRR, Arputharaj K. A novel supervised approach for segmentation of lung parenchyma from chest CT for computer-aided diagnosis. *J Digit Imaging* 2013;26:496–509.
- [54] Choukri D, Mehdi A. A new predictive approach to variables selection through genetic algorithm and fuzzy adaptive resonance theory using medical diagnosis as a case. The 8th International Conference on Ambient Systems, Networks and Technologies (ANT2017). 2017. pp. 448–57.
- [55] Kaushik D, Singh U, Singhal P, Singh V. Medical image segmentation using genetic algorithm. *Int J Comput Appl* 2013;81:10–5.
- [56] Hole KR, Gulhane VS, Shellockar ND. Application of Genetic algorithm for image enhancement and segmentation. *Int J Adv Res Comput Eng Technol* 2013;2:1342–6.
- [57] Girish C, Ferat S. A survey on feature selection methods. *Comput Electr Eng* 2014;40:16–28.
- [58] Canny J. A computational approach to edge detection. *IEEE Trans Pattern Anal Mach Intell* 1986;8:679–98.
- [59] Abo-Zahhad M, Gharieb RR, Ahmad SM, Donkol AAE. Edge detection with a preprocessing approach. *J Signal Inf Process* 2014;5:123–34.
- [60] Rafati M, Arabfard M, Rafati-Rahimzadeh M. Comparison of different edge detections and noise reduction on ultrasound images of carotid and brachial arteries using a speckle reducing anisotropic diffusion filter. *Iran Red Crescent Med J* 2014;16:1–9. <http://dx.doi.org/10.5812/ircmj.e14658>
- [61] Frasio I, Borghese NA. Statistical based impulsive noise removal in digital radiography. *IEEE Trans Med Imaging* 2009;28:1–16.
- [62] Eftekhari Moghadam A, Mardani M, Hasanzadeh H, Rafati M. Assessment of absorbed dose in critical organs in OPG: a phantom study. *J Paramed Sci* 2015;6:44–9.
- [63] Rafati M, Arabfard M, Rafati Rahimzadeh M, Voshtani H, Moladoust H. A comparison study of three speckle reducing methods for intima-media thickness ultrasound images. *Iran Red Crescent Med J* 2015;17:1–8. <http://dx.doi.org/10.5812/ircmj.e2513>
- [64] Sivakumar R, Gayathri MK, Nedumaran D. Speckle filtering of ultrasound B-mode images – a comparative study single scale spatial adaptive filters, multiscale filter and diffusion filters. *Int J Eng Technol* 2010;2:514–23.
- [65] Kumar N, Kumar S. Image quality assessment techniques. *Int J Adv Res Comput Sci Softw Eng* 2013;3:636–40.
- [66] Varan CS, Jagan A, Kaur J, Jyoti D, Rao DS. Image quality assessment techniques pn spatial domain. *Int J Comput Sci Technol* 2011;2:177–84.
- [67] Wang Z, Sheik HR, Bovik AC. No-reference perceptual quality assessment of JPEG compressed images. *Proc ICIPo2*, vol. 1. 2002;p. 477–80.
- [68] Available at: <http://sipi.usc.edu/database/database.php>.
- [69] Available at: <http://www.o.ntust.edu.tw/cweiwang/ISBI2015>.
- [70] Wang CW, Huang CT, Lee JH, Li CH, Chang SW, Siao MJ, et al. A benchmark for comparison of dental radiography analysis algorithms. *Med Image Anal* 2016;31:63–76.
- [71] Chugh T, Jain AK, Jaiswal RK, Mehrotra P, Mehrotra R. Bone density and its importance in orthodontics. *J Oral Craniofac Res* 2013;3:92–7.
- [72] Govindraju P, Chandra P. Radiomorphometric indices of mandible – an indicator of osteoporosis. *J Clin Diagn Res* 2014;8:195–8.
- [73] Le T, Chartrand R, Asaki TJ. A variation approach to reconstructing images corrupted by Poisson noise. *J Math Imaging Vis* 2007. <http://dx.doi.org/10.1007/s10851-007-0652-y>
- [74] Shruthi G, Usha BS, Sandya S. A novel approach for Speckle reduction and enhancement for ultrasound images. *Int J Comput Appl* 2012;45:14–20.
- [75] Saxena C, Kourav D. Noises and image denoising techniques: a brief survey. *Int J Emerg Technol Adv Eng* 2014;4:878–85.
- [76] Karthikeyan K, Chandrasekar C. Speckle noise reduction of medical ultrasound images using Bayesshrink wavelet threshold. *Int J Comput Appl* 2011;22:8–14.
- [77] Rajan J, Kannan K, Kaimal MR. An improved hybrid model for molecular image denoising. *J Math Imaging Vis* 2008;31:73–9.

- [78] Strong D, Chan T. Edge-preserving and scale-dependent properties of total variation regularization. *Inverse Probl* 2003;19:165–87.
- [79] Raj VNP, Venkateswarlu T. Denoising of medical images using total variation method. *Signal Image Process* 2012;3:131–42.
- [80] Khursheed S, Khaliq AA, Malik SA, Shah JA, Khan S. Poisson noise removal using wavelet transform. *Sci Int (Lahore)* 2014;27:287–92.
- [81] Avhad S, Patil RA. Denoising techniques for biomedical images. *Int J Eng Res Gen Sci* 2016;4:706–10.
- [82] Beg AH, Islam MZ. Advantages and limitation of genetic algorithms for clustering records. *IEEE 11th conference on Industrial Electronics and Applications*. 2016. pp. 2478–83.
- [83] Foi A, Trimeche M, Katkovonik V, Egiazarian K. Practical Poissonian-Gaussian noise modeling and fitting for single-image raw-data. *IEEE Trans Image Process* 2008;17:1737–54.
- [84] Luisier F, Blu T, Unser M. Image denoising in mixed Poisson-Gaussian noise. *IEEE Trans Image Process* 2011;20:696–708.
- [85] Bansal B, Saini JS, Bansal V, Kaur G. Comparison of various edge detection techniques. *J Inf Oper Manag* 2012;3:103–6.
- [86] Makitalo M, Foi A. Optimal inversion of the Anscombe transformation in low-count Poisson image denoising. *IEEE Int Trans Image Process* 2010;20:99–108.
- [87] Hessianian S, Arefi H. Assessment of restoration methods of X-ray images with emphasis on medical photogrammetric usage. *Int Arch Photogramm Remote Sens Spat Inf Sci* 2016; XLI-B5:835–40.
- [88] Borges LR, de Oliveira HCR, Nunes PF, Bakic PR, Maidment ADA, Vieira MAC. Method for simulating dose reduction in digital mammography using the Anscombe transformation. *Med Phys* 2016;43:2704–14.
- [89] Fan Z, Sun Q, Ji Z, Ruan F, Zhao L. An image filter arithmetic based on GA, PDE, and TV. *Int J Future Gen Commun Netw* 2013;6:147–56.